remote sensing

MDPI

Article

Estimating Subcanopy Solar Radiation Using Point Clouds and GIS-Based Solar Radiation Models

Daniela Buchalová [1,*], Jaroslav Hofierka [1], Jozef Šupinský [1] and Ján Kaňuk [2]

[1] Institute of Geography, Faculty of Science, Pavol Jozef Šafárik University in Košice, 04154 Kosice, Slovakia; jaroslav.hofierka@upjs.sk (J.H.); jozef.supinsky@upjs.sk (J.Š.)
[2] Photomap, s.r.o., Poludníková 3/1453, 04012 Kosice, Slovakia; jan.kanuk@photomap.sk
* Correspondence: daniela.buchalova@student.upjs.sk

Abstract: This study explores advanced methodologies for estimating subcanopy solar radiation using LiDAR (Light Detection and Ranging)-derived point clouds and GIS (Geographic Information System)-based models, with a focus on evaluating the impact of different LiDAR data types on model performance. The research compares the performance of two modeling approaches—r.sun and the Point Cloud Solar Radiation Tool (PCSRT)—in capturing solar radiation dynamics beneath tree canopies. The models were applied to two contrasting environments: a forested area and a built-up area. The r.sun model, based on raster data, and the PCSRT model, which uses voxelized point clouds, were evaluated for their accuracy and efficiency in simulating solar radiation. Data were collected using terrestrial laser scanning (TLS), unmanned laser scanning (ULS), and aerial laser scanning (ALS) to capture the structural complexity of canopies. Results indicate that the choice of LiDAR data significantly affects model outputs. PCSRT, with its voxel-based approach, provides higher precision in heterogeneous forest environments. Among the LiDAR types, ULS data provided the most accurate solar radiation estimates, closely matching in situ pyranometer measurements, due to its high-resolution coverage of canopy structures. TLS offered detailed local data but was limited in spatial extent, while ALS, despite its broader coverage, showed lower precision due to insufficient point density under dense canopies. These findings underscore the importance of selecting appropriate LiDAR data for modeling solar radiation, particularly in complex environments.

Keywords: solar radiation model; LiDAR; forest canopy; GIS; beam radiation; subcanopy solar radiation

Academic Editor: Eben N. Broadbent

Received: 20 November 2024
Revised: 23 December 2024
Accepted: 14 January 2025
Published: 18 January 2025

Citation: Buchalová, D.; Hofierka, J.; Šupinský, J.; Kaňuk, J. Estimating Subcanopy Solar Radiation Using Point Clouds and GIS-Based Solar Radiation Models. *Remote Sens.* **2025**, *17*, 328. https://doi.org/10.3390/rs17020328

1. Introduction

The spatial distribution of solar radiation on land surface is driven by many factors, such as latitude, topography, atmospheric situation, and vegetation [1–3]. The vegetation canopy significantly influences solar radiation, as tree crowns absorb a large portion of the incoming solar radiation. However, depending on the canopy's density, some fraction of the sunlight still reaches the ground. This reduction in solar radiation below the canopy is manifested especially in the beam (direct) component of solar radiation which is usually the largest component of the global solar radiation during clear sky atmospheric conditions. The reduction is also evident in a diffuse component, which is anisotropic and related to beam solar radiation [4].

Vegetation represents a complex data structure. Physical aspects such as form, height, density, branching structure, and leaves are the main components that create shade and important variables characterizing the light conditions inside the stand, and under the

treetops [1,5–10]. These structural elements significantly influence the accuracy of solar radiation modeling, necessitating high-resolution data to capture fine-scale interactions between vegetation and solar radiation.

Traditional methods of quantifying solar radiation are performed either directly (e.g., using quantum sensors) or indirectly (e.g., with hemispherical photography). Comprehensive reviews on the quantification of forest light environments, focusing on tools, methods, accuracy, and costs, have been published by many authors, e.g., [6,11,12]. However, these reviews do not address the use of remote sensing technology. The issue of modeling solar radiation in the forest using remote sensing data is present in a review study by Olpenda et al. [13].

LiDAR (Light Detection and Ranging) technology, including airborne laser scanning (ALS), terrestrial laser scanning (TLS), and unmanned aerial system laser scanning (ULS), has revolutionized the collection of high-resolution 3D data on forest and urban canopies. ALS provides broad coverage, making it suitable for large-scale studies, but its lower point cloud density can limit its ability to capture fine canopy details. In contrast, TLS and ULS generate high-density point clouds, enabling detailed analysis of canopy gaps, understory vegetation, and shading patterns [14–16]. Wu et al. [17] demonstrated that ALS excels at capturing top-of-crown metrics such as crown area and height in horticultural crops, while TLS provides superior accuracy for metrics that rely on lower canopy structures, such as crown volume and vertical leaf area profiles. These findings underscore the importance of selecting the appropriate LiDAR technology based on the application and structural complexity of the environment. Similarly, Neuville et al. [18] highlighted the potential of Unmanned Aerial Vehicle (UAV) LiDAR in dense forest stands, particularly for detecting tree stems and estimating Diameter at Breast Height (DBH), even under challenging leaf-on conditions. These studies illustrate how the choice of LiDAR platform affects the spatial resolution, coverage, and ability to capture fine structural details.

For example, the integration of UAV LiDAR for urban and forest applications has demonstrated significant potential in studies by Li et al. [19] and Moudrý et al. [20]. Much of the research on modeling solar radiation under tree canopies has utilized LiDAR and photogrammetry [13,21–23]. Currently, these methods are the most effective ways of data collection, enabling high spatial resolution of landscape features [14,15,24]. LiDAR provides high-resolution 3D point clouds of forest structures, allowing detailed analysis of canopy gaps and understory vegetation. Photogrammetry, especially with the advent of UAVs, has also been used to capture high-resolution images for the 3D reconstruction of forest environments. Methods such as Structure from Motion (SfM) produce dense point clouds that, while less accurate than LiDAR, offer a cost-effective alternative for large-scale applications [25].

Several studies have demonstrated the potential of LiDAR and photogrammetry-based methods for modeling solar radiation under tree canopies. For example, Witzmann et al. [26] introduced an algorithm that utilizes terrestrial LiDAR point clouds to estimate potential solar radiation reaching the forest floor. This approach transforms point clouds into a coordinate system aligned with solar rays, calculates the path length of sunlight through the canopy, and applies Beer's law to quantify radiation attenuation. Validation using hemispherical photographs and Solariscope measurements confirmed the accuracy of this method, highlighting its utility for ecological and silvicultural applications. Similarly, Xue et al. [27] developed a synergistic approach combining airborne LiDAR and computer graphics to model radiant fluxes in forest plots. By simulating solar beams and their interactions with canopy surfaces, this method demonstrated strong agreement with hemispherical photo-based and pyranometer measurements, providing a robust framework for analyzing spatiotemporal variations in solar radiation. Zhang et al. [28] and Sahu and

Jena [29] further explored the use of fisheye photography for capturing canopy structures and estimating subcanopy solar radiation. Their findings underscore the effectiveness of fisheye photographs in representing canopy heterogeneity and calculating light conditions beneath the canopy. Despite some limitations in accuracy due to mismatched observation conditions, these studies highlight the utility of combining photographic techniques with algorithmic modeling for understanding subcanopy radiation dynamics.

Solar radiation models aim to quantify the amount of solar energy reaching various layers of the forest canopy, taking into account factors such as the sun's angle, atmospheric conditions, and the structural complexity of the canopy. Traditional models like r.sun [30], implemented in the GRASS GIS environment [31], are designed for raster data and excel in large-scale or regional studies where computational efficiency and simpler data structures are required. Tools such as Solar Analyst [32] also rely on raster data and have been widely used for similar applications. These raster-based models are particularly effective in urban environments where canopy structures and terrain are less complex, allowing for accurate solar radiation predictions with minimal preprocessing. In contrast, recent advancements have focused on utilizing high-resolution 3D point cloud data for solar radiation modeling. The Point Cloud Solar Radiation Tool (PCSRT) [33] transforms point cloud data into voxel grids, enabling detailed analysis of solar radiation dynamics in environments with heterogeneous canopy structures, such as dense forests. By accounting for fine-scale shading effects and light attenuation, PCSRT offers a level of precision that surpasses traditional raster-based methods, particularly in complex forested settings. The choice between r.sun and PCSRT reflects the trade-offs inherent in their design; r.sun prioritizes computational efficiency and simplicity, making it ideal for studies requiring broad spatial coverage with straightforward data processing requirements. Conversely, PCSRT emphasizes precision and the ability to capture detailed subcanopy dynamics, albeit with higher computational and memory demands. Empirical models, often based on ground measurements, remain critical for validating both approaches, as highlighted by Parker et al. [34]. Their study underscores the importance of field data in understanding the intricate interactions between canopy structure and light transmission, which are central to both raster-based and voxel-based modeling approaches.

Modeling subcanopy solar radiation is vital for understanding forest ecosystems; yet, it remains a complex challenge due to the variability in light penetration. The integration of GIS (Geographic Information System) and LiDAR has significantly enhanced these models by improving spatial resolution. GIS enables large-scale spatial analysis, while LiDAR provides high-resolution data on canopy structure, allowing for more accurate light distribution modeling within forest canopies [13].

This paper explores two approaches to modeling solar radiation beneath tree canopies, each based on different input data sources. The first approach utilizes the r.sun model, which requires raster data, while the second approach employs the PCSRT model, which uses point clouds. Both approaches use the same solar radiation modeling principles based on the European Solar Radiation Atlas (ESRA) model [30,33], but they differ significantly in their data requirements and capacity to represent subcanopy environments. Therefore, the goal of this study is to compare these modeling approaches, assess their accuracy in predicting solar radiation under tree canopies represented by point clouds collected by different LiDAR data sources, and analyze the impact of different input data types on model performance.

2. Methods and Data

2.1. Solar Radiation Models

2.1.1. r.sun

The r.sun solar radiation model calculates two-dimensional (2D) raster maps of direct, diffuse, and reflected radiation for a specific day, latitude, surface, and atmospheric conditions [30]. The r.sun model is implemented in the GRASS GIS v7.8.7 software as the r.sun module [35]. It is based on the European Solar Radiation Atlas (ESRA) model [36]. The r.sun module operates in two modes: the first mode calculates the angle of incidence of the sun and solar irradiance (W/m^2) at a specific time of day, and the second mode calculates the global solar radiation (Wh/m^2) for a specific day of the year. Both modes calculate global solar radiation with its three components—beam, diffuse, and reflected solar radiation—based on time, location, topography, and atmospheric conditions. The input data include a raster of elevations and a day of the year. Location values are provided by latitude and longitude grids or through internal calculations. Shading is calculated internally or using horizon raster maps generated by the r.horizon module in GRASS GIS. The slope, aspect ratio, Linke turbidity coefficient, and albedo parameters can be provided as uniform values or spatially variable rasters. A detailed description, parameters, notes, and examples are available in the GRASS GIS manual [35] and in the book by Neteler and Mitasova [31].

In the r.sun module, the clear-sky solar radiation can be attenuated by the coeff_bh and coeff_dh raster-based parameters to calculate the real-sky radiation by estimating the influence of clouds or haze. The coeff_bh and coeff_dh input raster maps define the fraction of the respective clear-sky radiations reduced by attenuation factors. The values of real-sky coefficients are in the range of 0–1. The same principle can be used for the estimation of attenuation of clear-sky solar radiation by the canopy via Leaf Area Index (LAI) or Light Penetration Index (LPI). The LPI metric assesses the extent to which light penetrates through a canopy. LPI is typically calculated as the ratio of light that passes through the canopy to the light available above the canopy. The LPI used in this study to estimate the attenuation of beam radiation via the coeff_bh parameter is calculated from the classified LiDAR data by dividing the number of ground hits (points) by the total number of hits.

The primary input for solar radiation modeling is the Digital Surface Model (DSM) which includes elevation, slope, and aspect rasters. The calculation of irradiance values for this study requires the specification of a day of the year and a local (solar) time provided in the decimal system. Another crucial input parameter is the Linke turbidity coefficient usually estimated for the given environment and atmospheric conditions.

2.1.2. Point Cloud Solar Radiation Tool

The PCSRT software is used for three-dimensional (3D) solar radiation modeling using voxelized point clouds [33]. PCSRT implements a developed method for modeling solar radiation in a 3D space represented by a volume grid. It can be used for objects represented by point clouds produced by a laser scanner or other methods. It is especially useful for highly fragmented areas, such as those covered by vegetation. The tool converts the point cloud coordinate system into a voxel-based system, where voxels have a uniform size, shape, and volume [33]. Similarly, to r.sun, PCSRT calculates beam, diffuse, and global solar radiation using the ESRA model for every point. The PCSRT transforms the input point cloud into a volume grid, constructs regression planes for each voxel based on surrounding points, and then calculates the insolation time and solar radiation components for the specified period. The Sun's position is calculated based on a reference point, ideally the

centroid of the point cloud. Currently, LAS and LAZ file formats are supported as input files, and LAS, LAZ, and PLY are supported as output files.

The tool is implemented using the Rust programming language, and after compilation, it can be run on any commonly used operating system (Windows, Linux, and MacOS). The solar radiation modeling method using the PCSRT aims to minimize the number of necessary input parameters and strives for the universality of use and calculation efficiency. The input data for the tool is a processed and optimized point cloud using other software tools such as CloudCompare v2.12.4. PCSRT is a command-line tool that requires at least the point cloud centroid position (latitude, longitude), Linke turbidity factor, and time period to be specified in addition to the input and output file paths. However, additional optional parameters can be used to modify how PCSRT processes the point cloud. The most "sensitive" parameters are the Linke turbidity factor, which has a direct impact on the output solar radiation values, and voxel size, which determines the level of detail in which the cloud is processed. The resolution limits the level of detail of the trees. If a voxel is too large, it causes the shadowing of other voxels located behind it and blocks the sun's rays. Conversely, if the voxel is too small, the voxel structure can allow sunlight to pass through the trunk or branches of trees, leading to inaccuracies. A detailed analysis of voxel size selection is provided by the authors of PCSRT in [33]. In this study, voxel sizes were set to 0.05 m for TLS and ULS data and 0.8 m for ALS data for both areas, reflecting the respective data densities.

2.1.3. Quantitative Comparison of Models

A quantitative comparison of PCSRT and r.sun was conducted to evaluate their input requirements, preprocessing demands, and computational efficiency. The computational experiments and model simulations were conducted on a system equipped with an Intel(R) Core(TM) i7-4790 CPU operating at 3.60 GHz. The system uses a 64-bit operating system with an x64-based processor architecture. The processor featured 8 cores, allowing for efficient parallel processing. The system was supported by 32.0 GB of DDR3 RAM.

PCSRT requires voxelization of point cloud data, enabling high-resolution subcanopy modeling but significantly increasing processing time and memory usage. In contrast, r.sun utilizes raster DSMs, which require minimal preprocessing and are computationally less intensive. Benchmarking experiments revealed that PCSRT required approximately 6 min to process TLS data (forested area), compared to 5 s for r.sun using a raster DSM. Memory usage for PCSRT was 23 GB, reflecting the additional computational complexity of voxelized data, while r.sun required significantly less memory.

2.2. Study Areas and Input Parameters

The study areas were selected to provide a realistic representation of typical environments in Central Europe. We have selected two study areas representing distinct landscape types with tree canopies: forested and built-up/urban landscapes (Figure 1). Each landscape exhibits unique structural characteristics. In forests, tree canopies play a dominant role in regulating the amount of solar radiation that reaches the ground. In contrast, urban landscapes are characterized by a diversity of structures, including buildings with various roof types and other constructions. Trees are also a vital and integral part of urban areas, but their spatial arrangement differs significantly from that in forests.

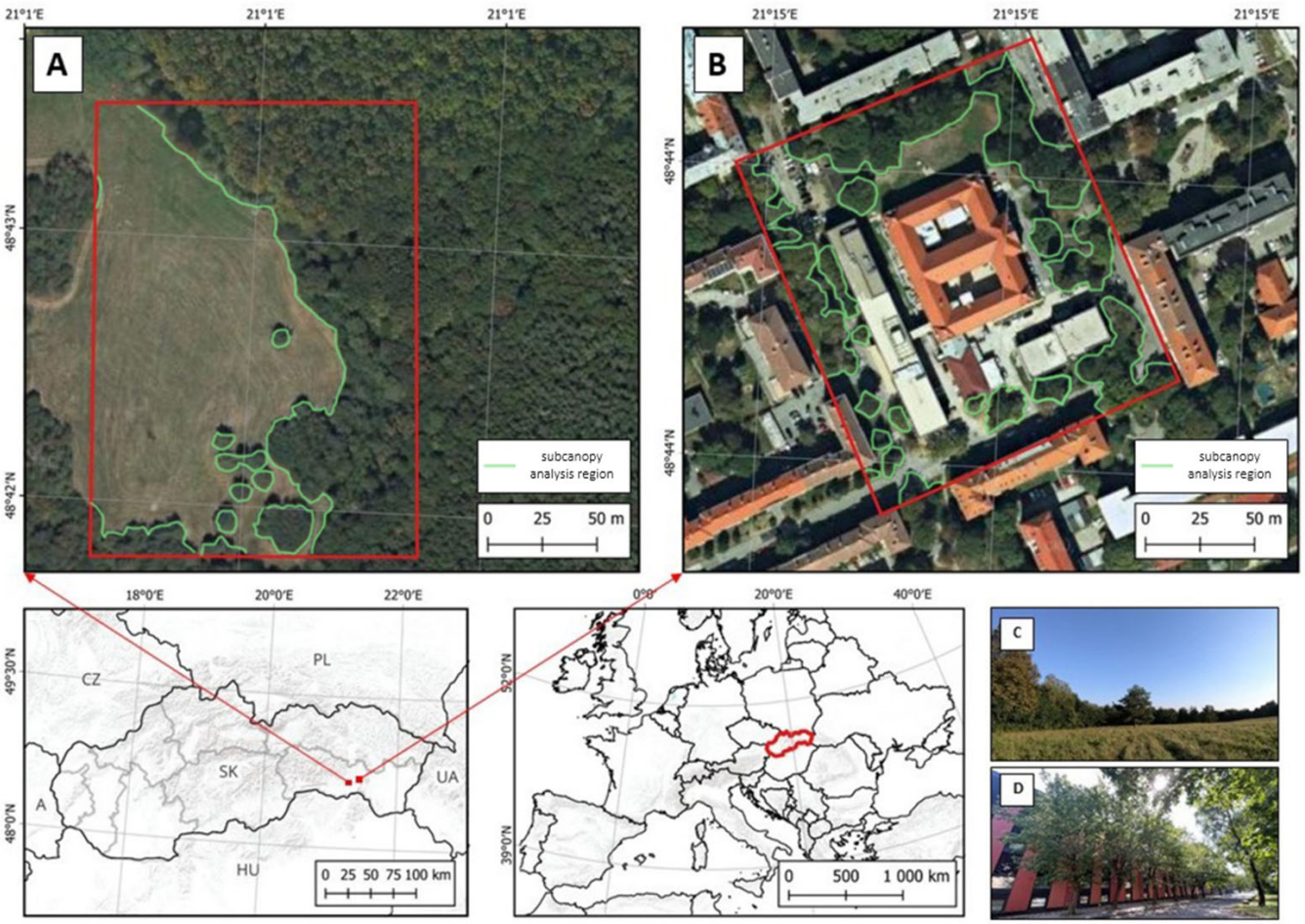

Figure 1. Locations of study areas. (**A**): Forested area; (**B**): built-up area; (**C**): side view of the forested area; (**D**): side view of the built-up area—Jesenná Street. Green lines indicate canopy areas.

The forested area with adjacent grassland near the village of Rudník is located in the Košice-okolie district in eastern Slovakia (48°42′32″N 21°01′15″E) at an altitude of 314 m above mean sea level. The forested area was chosen to represent a typical Central European deciduous forest, characterized by a mixed-species canopy structure that provides a diverse range of canopy densities and light penetration conditions. This area was selected for its species diversity and structural variability, which are reflective of regional forest ecosystems. The deciduous forest in the selected area consists of various types of trees typical for the Central European region including beech (*Fagus sylvatica*), sessile oak (*Quercus petraea*), pedunculate oak (*Quercus robur*), white ash (*Fraxinus excelsior*), and sycamore maple (*Acer pseudoplatanus*). In addition to these in the selected area, we also identified small islands of coniferous trees, specifically Scots pine (*Pinus sylvestris*). The forest consists of approximately 80% deciduous species and 20% coniferous species, capturing the mixed-species nature of the region. Tree heights in this area have a mean of 18.2 m (±4.6 m), with values ranging from 10 m in younger stands to 28 m in mature stands.

The urban area, on the other hand, was selected to represent a typical built-up environment in a mid-sized Central European city, characterized by varied building heights and scattered vegetation, including ornamental trees. The built-up area is located in the central part of the city of Košice (48°42′32″N 21°01′15″E) at an altitude of 210 m above sea level. The area includes segments of Jesenná, Jilemnického, and Park Angelinum streets. Since this is an urban area, the selected location contains various types of trees typical for urban environments and urban planning such as box elder (*Acer negundo*), silver

birch (*Betula pendula*), and *Norway spruce* (*Picea abies*), among others. Within the selected area, there are several buildings, including a university building, residential buildings, and technical buildings. In the urban area, vegetation distribution was described by tree density, which averages approximately 5 trees per hectare, and species diversity, which includes 12 dominant tree species with variable crown structures. The urban vegetation also features frequent canopy gaps due to built structures, creating heterogeneous solar radiation conditions within the area. This variability in canopy cover and structure ensures the urban area is representative of typical urban environments in the region, characterized by a mix of vegetation and infrastructure.

The input parameter for solar radiation modeling using r.sun was the elevation raster map representing DSM, created in the CloudCompare software v2.12.4 with a resolution of 0.5 m. Additional input parameters included the slope and aspect raster maps derived from DSM. The module operates using a specific day of the year: for the built-up area, it was the 271st day of the year, and for the forested area, it was the 272nd day of the year. We analyzed 2 days with clear-sky conditions to ensure consistent atmospheric and solar input parameters. Time was specified in solar (local) time.

The Linke turbidity factor values used in the study were obtained from the SoDa1 database, a comprehensive resource for atmospheric and solar radiation data [37]. Since no meteorological measurements of the Linke turbidity factor were available for the study areas, the selection of these values for the particular day was further refined through calibration against pyranometer measurements conducted in the study areas. Solar radiation was modeled for the specified day and time, and the modeled values were adjusted to align with observed pyranometer readings.

For the built-up area, a Linke turbidity factor value of 3 was determined, reflecting typical atmospheric conditions for urban environments in the northern hemisphere during September. Conversely, a lower value of 2.5 was applied to the forested area, representing a rural setting with minimal air pollution and aligning with established values for clear-sky conditions. To ensure consistency, these values were applied uniformly across all models, maintaining compatibility with local seasonal conditions and adhering to established solar radiation modeling principles.

The input parameters for solar radiation modeling using PCSRT for the forested area data were set as follows: the point cloud centroid's geographical coordinates, the time range, in RFC3339 format, was defined as 2023-09-28T06:00:00.000Z to 2023-09-28T06:01:00.000Z, with a step interval of 1 min. The Linke turbidity factor was also set to 2.5. The voxel size was adjusted according to the type of input data. The input parameters for the built-up area data were set as follows: the point cloud centroid's geographical coordinate, the time range, in RFC3339 format, was defined as 2023-09-27T06:00:00.000Z,2023-09-27T06:01:00.000Z, with a step interval of 1 min. The Linke turbidity factor was also set to 3.

2.3. Data Collection Methods

Laser scanning, or LiDAR, is currently the most effective technique for mapping the geometric structure of landscapes [16,19]. It is an active remote sensing technique that emits laser pulses and records their reflections to create highly accurate point clouds of landscape features. The LiDAR method produces a point cloud that can be processed to create various data products, including vector models, Triangulated Irregular Network (TIN) or mesh models, and raster layers.

When it comes to efficiency in mapping large areas with high detail, aerial platforms such as manned aircraft and UAVs are particularly effective. Both platforms can carry LiDAR, but they produce different results due to varying operational parameters, such as altitude and speed. UAVs typically capture finer details, which is crucial for accurately modeling solar radiation beneath tree canopies, as the canopy structure greatly influences the transmission of sunlight. To complement aerial data, ground-based methods, particularly terrestrial laser scanning, are essential for achieving highly detailed point clouds.

Terrestrial and airborne laser scanning differ notably in the quality and detail of the point clouds they generate. Terrestrial laser scanning, conducted from a static tripod, provides a high-density point cloud near the scanner, allowing for detailed capture of tree canopies and the terrain beneath them. In contrast, airborne laser scanning relies on a mobile platform, where precise flight trajectory calculations are critical for accurate data. Modern software tools can correct errors resulting from positional uncertainties during data collection.

This study employs a combination of advanced laser scanning techniques to accurately capture the structural characteristics of both forested and built-up environments (Figure 2). Three different types of laser scanning technologies—terrestrial laser scanning, unmanned aerial system laser scanning, and aerial laser scanning—were used to obtain detailed point cloud data across the study areas. For the forested area, we used data from TLS, ALS, and ULS. For the built-up area, we used 2 types of data, data from TLS and ALS.

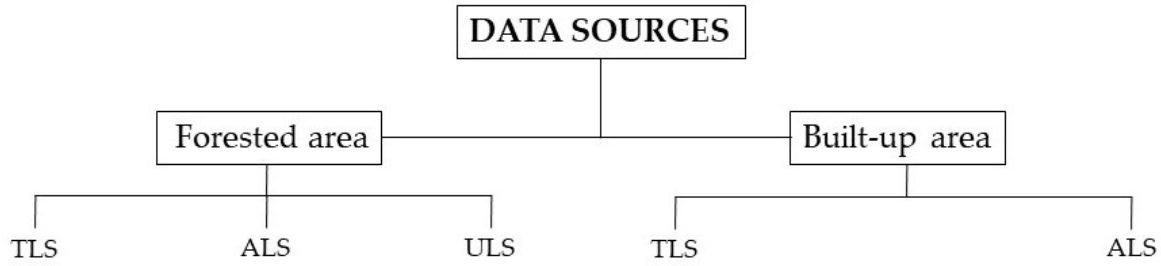

Figure 2. Data collection methods used in the study areas; TLS (terrestrial laser scanning), ALS (aerial laser scanning), ULS (unmanned laser scanning).

2.3.1. TLS

To obtain terrestrial laser scanning data, we used the Riegl VZ-1000 terrestrial laser scanner, which is well suited for mapping vegetation in both forested and urban landscapes. This 3D laser scanner offers a wide field of view with a 100° vertical and 360° horizontal range. The selected research areas, forested area, and built-up area were both mapped using TLS. For both sites, we employed the same scanning parameters: a frequency of 300 kHz with Panorama 40 mode, providing a 0.04° step for pulse emission in both horizontal and vertical directions. In the forested area, we performed 26 scanning positions, and in the built-up area, we conducted 30 scanning positions (Figure 3). The scanning positions were spaced within 25 m of each other, ensuring sufficient overlap, which is crucial for the accurate registration of individual scan positions.

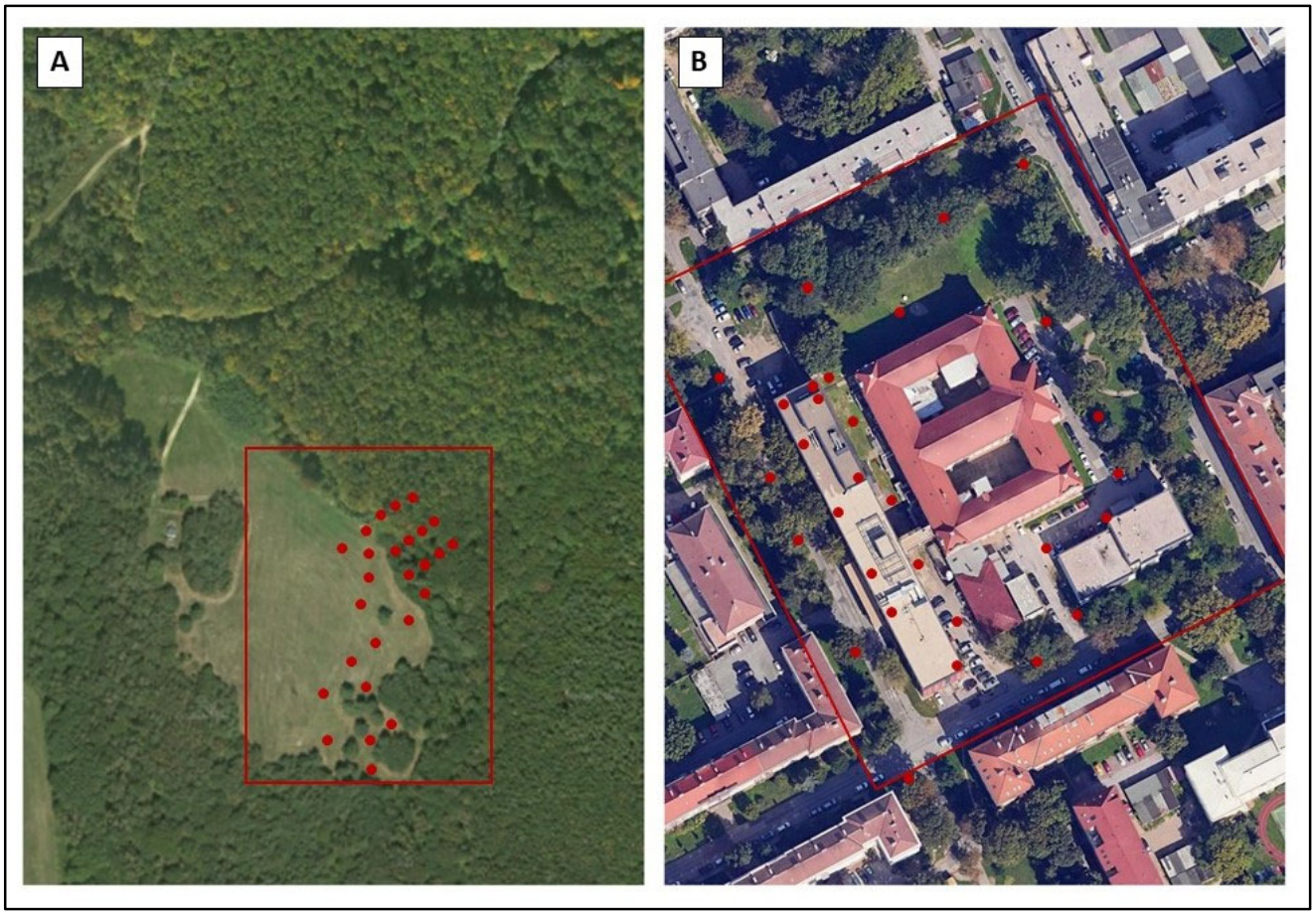

Figure 3. TLS positions in (**A**): forested area; (**B**): built-up area.

The registration of the individual scan positions was carried out using the RiSCAN Pro v2.9 software. In the initial step, noise was removed from the scan data based on the deviation parameter. This parameter helps identify points with a high likelihood of positional uncertainty—specifically, points whose trace deviates significantly from a perfect circle. Such points typically occur on grass, tree branches, or surfaces with sharp angles of incidence and could compromise the accuracy of the registration. In our case, we applied a deviation filter with a value of $\leq$20.

The second step involved coarse registration using four identical points, with the first scan position serving as the reference. After this, automatic registration was performed using the Multi-Station Adjustment (MSA) tool, with a plane patch filter applied. The resulting automatic registration error for aligning each scan position to a common coordinate system was 0.015 m.

To georeference the point cloud within a global coordinate system, we employed a straight-line registration method based on ground control points (GCPs). Photogrammetric targets were used to signal the GCPs, and their positions were recorded using the TOPCON HiPer HR GNSS system. The GCPs were captured using the RTK method with access to the SKPOS (Slovak real-time positioning service) network. A total of 8 GCPs were used for registration, resulting in a total registration error of 0.018 m. Finally, the point cloud was subsampled to a 0.02 m resolution using the "Spatial Sampling" filter in the CloudCompare software. This step removed duplicate and redundant points, significantly reducing computational demands for solar radiation modeling without compromising the accuracy of the final estimates.

In the forested area, TLS captured 58,528,112 total number of points (vegetation and ground) with 1353.44 average density per m^2 (Figure 4A). Of these, 13,195,446 points represent terrain, with a terrain point density of 333.66 points per m^2 (Figure 4B). Figure 4 shows the highest point densities near the TLS positions and within dense vegetation areas where the laser beam could capture more details due to the proximity and structure of the objects. Conversely, the point density decreases in open areas like the meadow, further away from the scanner, where fewer surfaces are available to reflect the laser pulses. The high density is due to the ground-based nature of TLS, which allows for detailed data collection of the lower canopy and forest floor. However, the density of the point cloud is affected by the number of scanning positions, which causes inhomogeneous data coverage (see Figure 4).

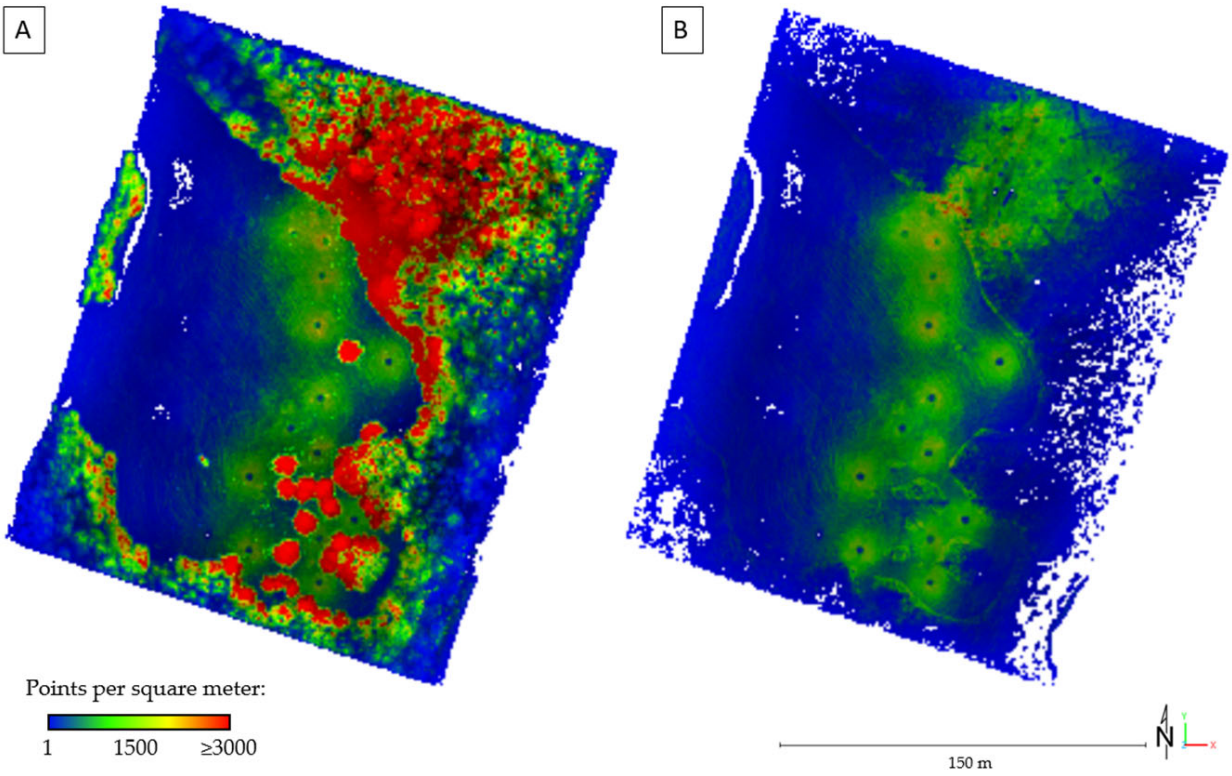

Figure 4. The TLS point cloud density in the forested area; (**A**): total points (vegetation and ground), (**B**): ground points.

In the built-up area, TLS captured a total number of points of 107,277,108 (vegetation and ground) with 3991.41 average density per m^2 (Figure 5A). Of these, 22,236,808 points represent terrain, with a terrain point density of 1102.02 points per m^2 (Figure 5B). The point cloud (Figure 5) shows typical TLS results for an urban environment, with the highest point density near the scanner positions, particularly on building facades and nearby objects. However, the density decreases with distance and occlusion, leading to varied distribution across the scene. While TLS provides high-resolution data, capturing intricate details of buildings and structures, the overall coverage is influenced by the number and placement of scanning positions, resulting in a non-uniform distribution of points.

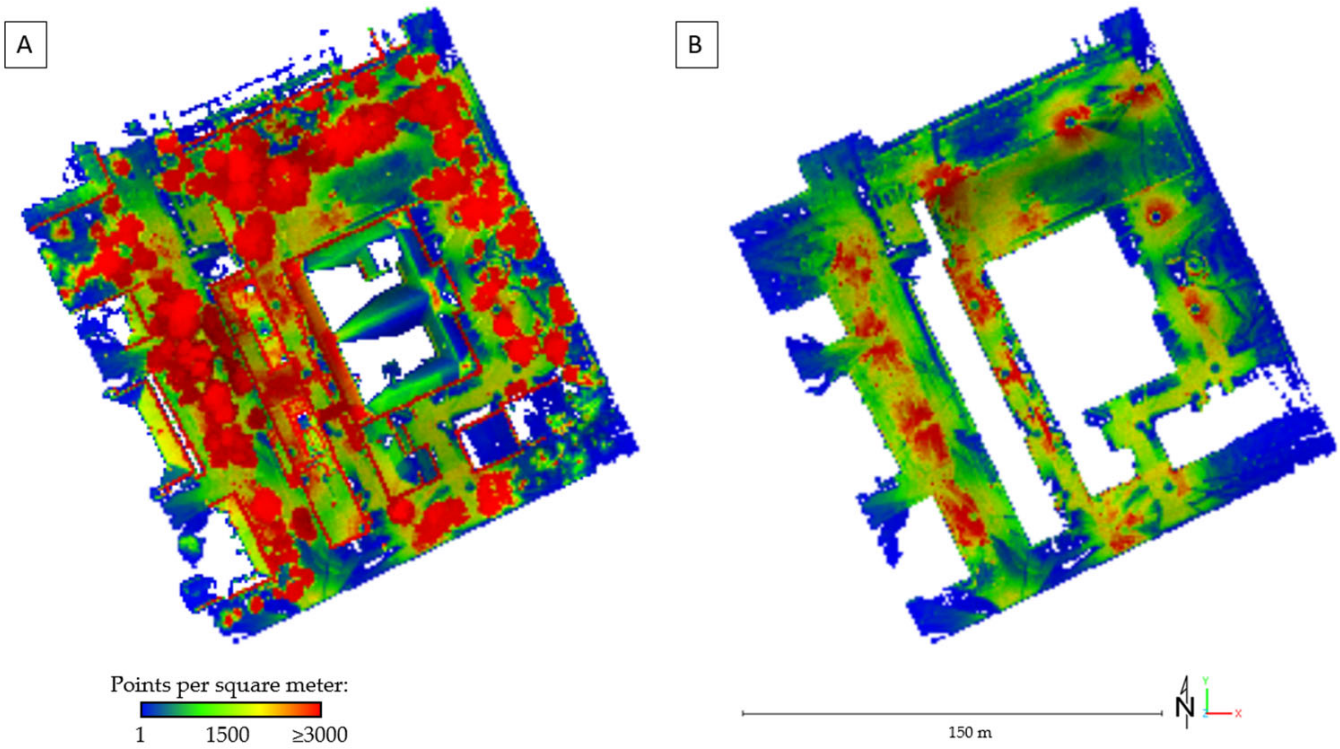

Figure 5. The TLS point cloud density in the built-up area; (**A**): total points (vegetation and ground), (**B**): ground points.

2.3.2. ULS

Another type of data used for modeling solar radiation under tree canopies is laser scanning data collected from UAVs. Due to local legislative restrictions on flying in built-up areas, these data were only available for the forested areas. Data collection at this area took place on 12 September 2023, at 08:14 UTC under clear weather conditions, with an air temperature of 26 °C and moderate winds up to 1 $m \cdot s^{-1}$.

For mapping, we utilized a unique laser system that integrated a modified DJI AGRAS T30 UAV carrier, a VUX-1 laser scanner, and an IMU OxTS xNAV 550 equipped with GNSS antennas from Novatel. The flight was conducted at an altitude of 60 m above ground level (AGL) with a speed of 3 $m \cdot s^{-1}$, and a scan rate of 550 kHz. The flight followed a double-grid flight plan. To reconstruct the flight trajectory and register the point cloud in the JTSK 03 coordinate system (EPSG code: 8353), corrections from a virtual base station derived from the SKPOS (Slovak real-time positioning service) system were applied in post-processing mode.

The flight trajectory was calculated using the Combined (Forwards + Backwards) processing method in the NAVsolve v3.12 software, with corrections applied for the corresponding epochs. The trajectory was exported at a recording rate of 100 Hz and imported into the RiPROCESS v1.8.6 software. Subsequently, the individual flight paths were exported using the rxp cutter tool, and systematic errors in the scanner's rotation angles were identified and corrected using the auto tie planes method. Each flight trajectory was then exported separately, and the StripAlignment v14.4 software from BAYES Solution was used to eliminate fluctuations in the point clouds. After alignment, the resulting data achieved an internal accuracy of 0.019 m.

The final step in processing the ULS data involved correcting the positioning error in the JTSK03 coordinate system using ground control points (GCPs). A total of 8 GCPs were used, marked by targets with dimensions of 0.3 × 0.3 m. These targets were surveyed

using the TOPCON HiPer HR GNSS system with the RTK method and access to the SKPOS network. The resulting point cloud accuracy was 0.021 m.

In the forested area, ULS captured 125,232,784 total number of points (vegetation and ground) with 2559.85 average density per m^2 (Figure 6A). Of these, 12,305,991 points represent terrain, with a terrain point density of 254.06 points per m^2 (Figure 6B). The point cloud shows (Figure 6) a dense canopy structure in the forested areas, leading to high point densities. Lower point density is on tree trunks and multiple levels of vegetation below the tree canopy ULS provides high-resolution spatial data and homogeneous coverage.

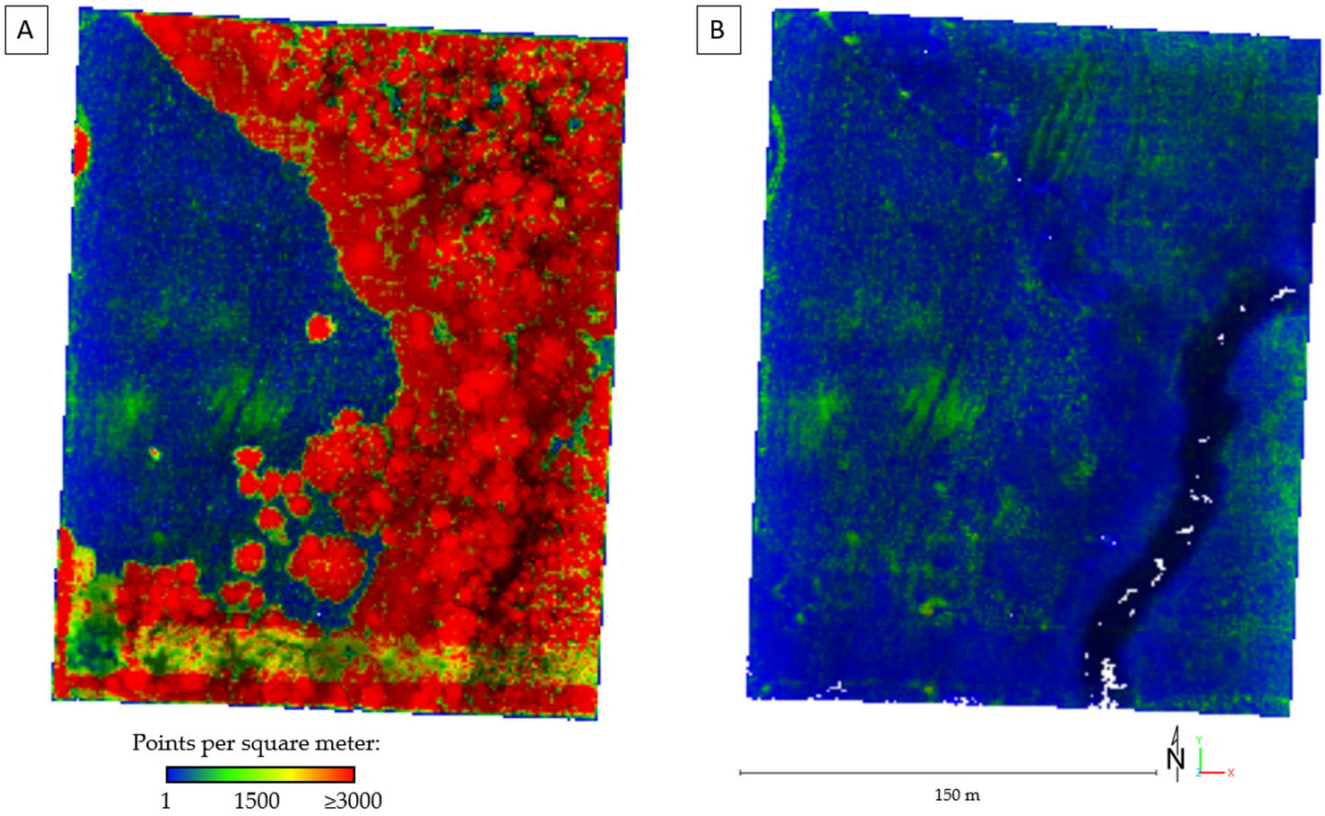

Figure 6. The ULS point cloud density in the forested area; (**A**): total points (vegetation and ground), (**B**): ground points.

2.3.3. ALS

ALS data were provided by the Office of Geodesy, Cartography, and Cadastre of the Slovak Republic (ÚGKK SR). Data collection took place during the vegetation-free period from 10 April 2021 to 26 April 2021, for both study areas. The reported height accuracy is 0.3 m (ETRS89-h) and positional accuracy is 0.09 m in ETRS89-TM34 [38].

In the forested area, ALS captures a total number of points of 1,718,408 (vegetation and ground) with a 20.38 average density per m^2 (Figure 7A). Of these, 1,069,650 points represent terrain, with a terrain point density of 12.71 points per m^2 (Figure 7B). ALS captures significantly fewer points and has the lowest average point cloud density. The lower point density is due to the higher altitude of ALS data collection, resulting in less detailed coverage, especially in complex vegetation structures.

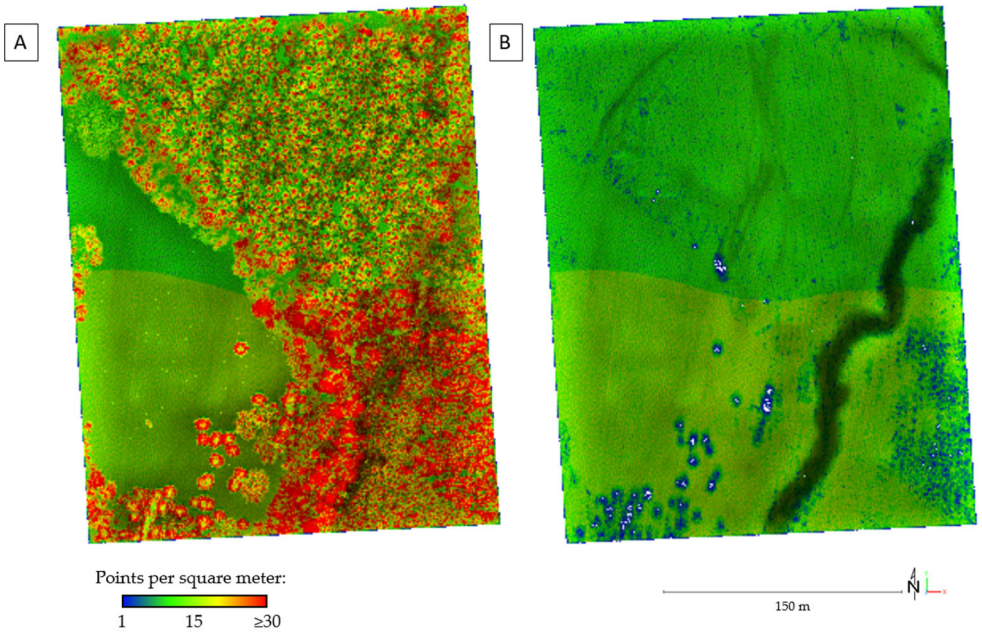

Figure 7. The ALS point cloud density in the forested area; (**A**): total points (vegetation and ground), (**B**): ground points.

In the built-up area, ALS captured a total number of points of 713,347 (vegetation and ground) with 23.08 average density per m^2 (Figure 8A). Of these, 383,995 points represent terrain, with a terrain point density of 16.93 points per m^2 (Figure 8B). The built-up areas, such as buildings, roads, and sidewalks, display a uniformly high point density, reflecting the effectiveness of LiDAR in capturing detailed surface information from man-made structures. The vegetated areas around the buildings show a more variable density, which corresponds to the complexity and heterogeneity of the natural environment. Trees and bushes, for example, cause varying levels of obstruction to the laser pulses, resulting in a mixed-density distribution. The edges of buildings and other structures might show slightly lower densities where the LiDAR pulses were at oblique angles, causing some data loss or scattering (see Figure 8). Although ALS provides uniform coverage of the area, the point density remains low.

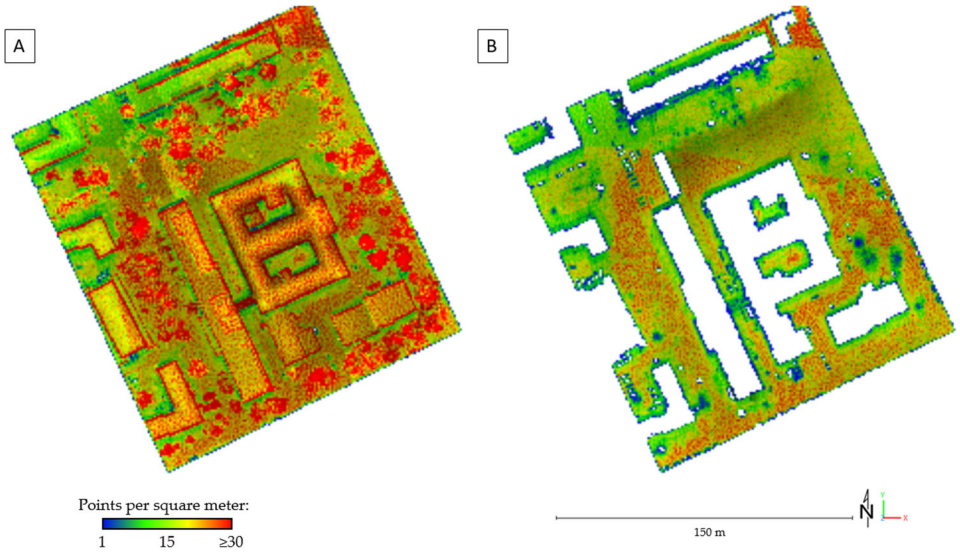

Figure 8. The ALS point cloud density in the built-up area; (**A**): total points, (**B**): ground points.

2.4. Preprocessing of LiDAR Data

To ensure the comparability of TLS, ULS, and ALS data during the experiments, a standardized preprocessing workflow was implemented. This workflow consisted of several steps designed to harmonize the datasets. First, all point clouds underwent an initial noise filtering process to remove outliers caused by scanning inaccuracies, with a uniform threshold applied across all datasets. Next, ground classification was performed, during which ground points were identified and separated from vegetation and other non-ground features using consistent ground-filtering algorithms applied uniformly to the TLS, ULS, and ALS datasets.

Additionally, TLS and ULS data for both built-up and forested areas were optimized to a resolution of 2.5 cm. This optimization step was necessary to address the large volume and high density of the data, which would otherwise impose excessive computational demands. Importantly, reducing the resolution to 2.5 cm did not compromise the quality or accuracy of the point clouds, ensuring the models retained sufficient detail for precise analysis. In contrast, ALS data were not optimized, as their lower initial density did not warrant further reduction.

The limited spatial extent of TLS data was addressed by focusing the analyses on small-scale areas with comprehensive TLS coverage. These areas were carefully selected to align with the overlapping ULS and ALS datasets. To ensure comparability, the larger-scale ULS and ALS datasets were clipped to match the spatial boundaries of the TLS coverage. This approach ensured that all models operated within the same spatial extent during the evaluation, facilitating consistent and reliable comparisons.

2.5. Validation

Validation of the results of solar radiation modeling was conducted using pyranometer measurements. A set of two MS-60 pyranometers with automatic data recording produced by the EKO-INSTRUMENTS company was used to measure solar radiation levels. The MS-60 is an ISO 9060:2018 Class B pyranometer with analog output and double dome construction for lower offsets and cosine errors. Validation measurements were carried out in the selected forested area over two days. On 27 September 2023, the validation measurement was conducted directly in the forest (see Figure 9C,D), while on 29 September 2023, it was conducted in a meadow with a free-standing coniferous tree (see Figure 9A,B). The measurements took place continuously between 9:30 a.m. and 4:50 p.m., with the amount of solar radiation recorded every minute. The two pyranometers were placed at selected locations approximately 10 m apart. The positions of the deployed pyranometers were recorded using a GPS device.

In the selected built-up area location, validation took place on 28 September 2023. The pyranometer was positioned on the roof of the Pavol Jozef Šafárik University building on Jesenná Street (Figure 10A). Placing a pyranometer sensor in a built-up area beneath tree canopies and around buildings is generally very challenging. In our area of interest, street corridors around the buildings experience heavy foot and motor vehicle traffic, making it impractical to place the sensor on sidewalks or streets. Another challenge in accurately measuring the amount of incident solar radiation around buildings is the reflection from surrounding surfaces, such as facades, windows, and parked cars. Modeling these reflections is complex because different materials exhibit varying reflectance properties. The measurements took place continuously between 8:45 a.m. and 6:00 p.m., with the amount of solar radiation recorded every minute. Given the public setting and frequent pedestrian activity in the area of interest, the pyranometer was not placed in vegetated areas.

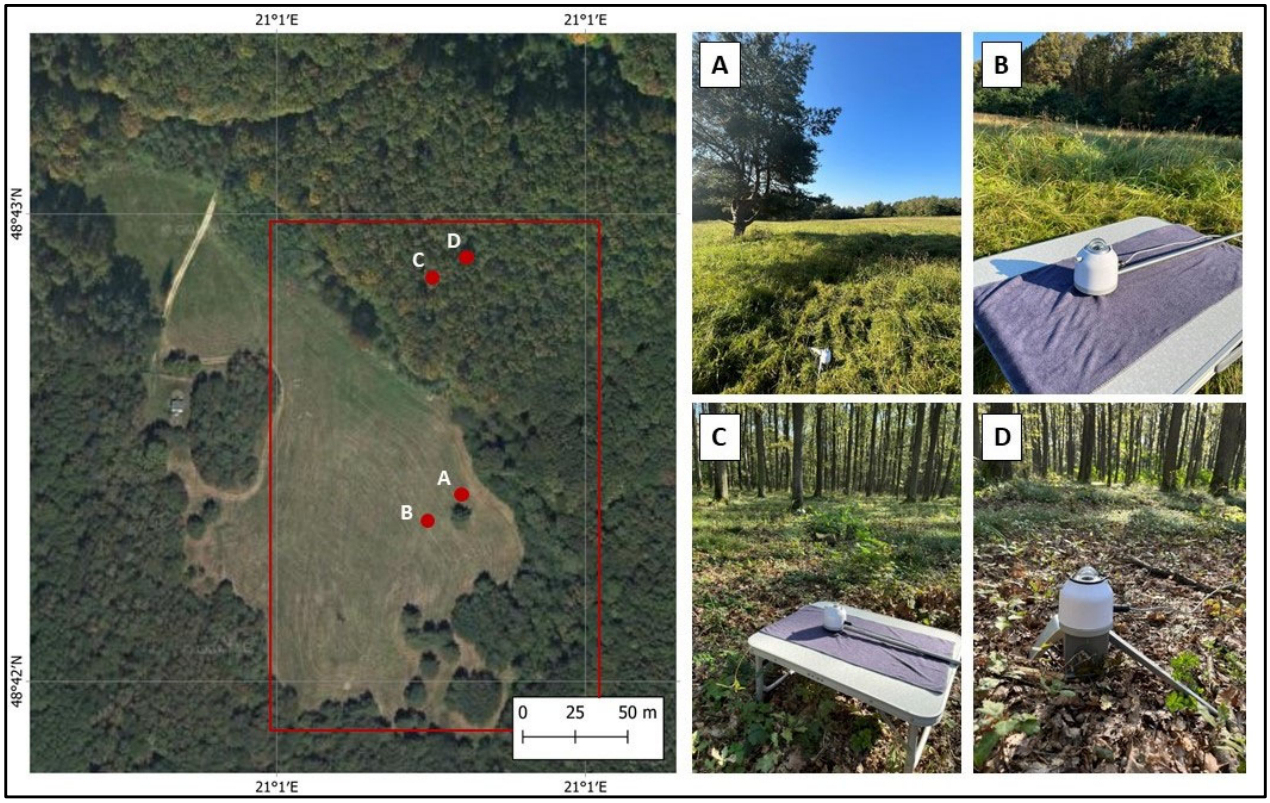

Figure 9. Localization of pyranometers in the forested area; (**A**): detailed photo of pyranometer in location A, (**B**): detailed photo of pyranometer in location B, (**C**): detailed photo of pyranometer in location C, (**D**): detailed photo of pyranometer in location D.

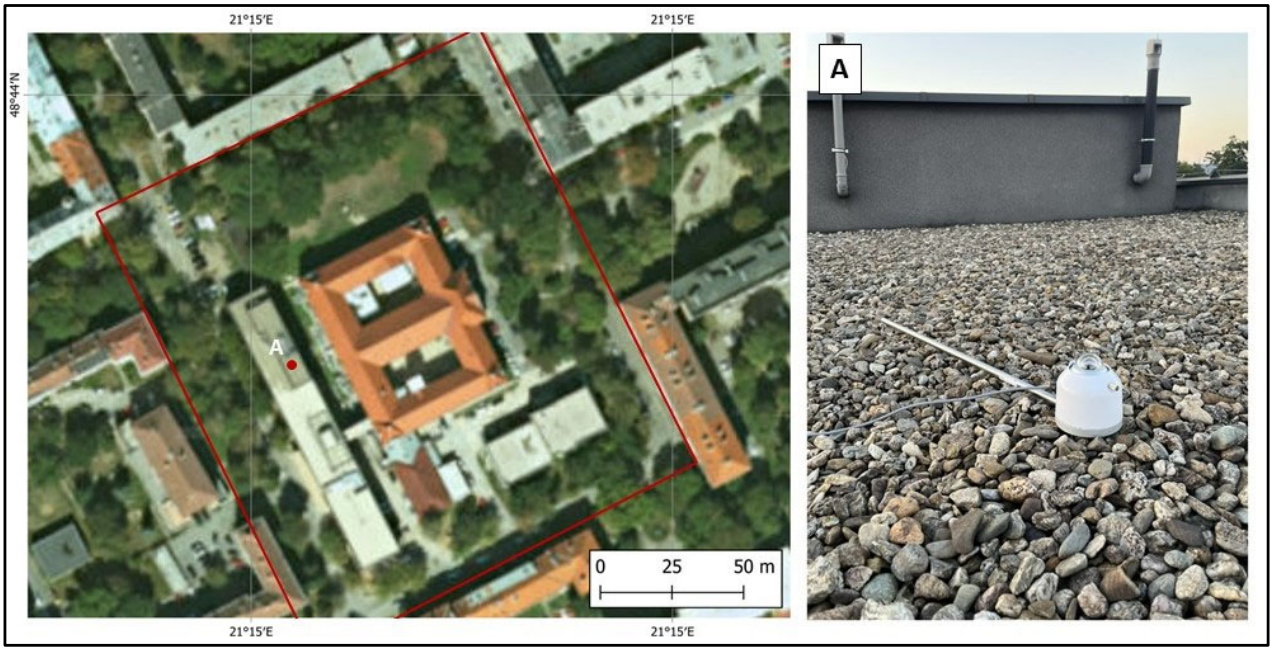

Figure 10. Localization of pyranometer in the built-up area; (**A**): detailed photo of pyranometer in location A.

3. Results

3.1. Point Clouds in the Forested Area

In the forested area, four distinct polygons (P1, P2, P3, and P4) were selected and used to analyze data derived from the ULS, ALS, and TLS datasets (Figure 11). Each polygon represents a specific type of vegetation or a forest structure, providing a basis for comparing data outputs from different scanning technologies. Polygons are 10 × 10 m in size.

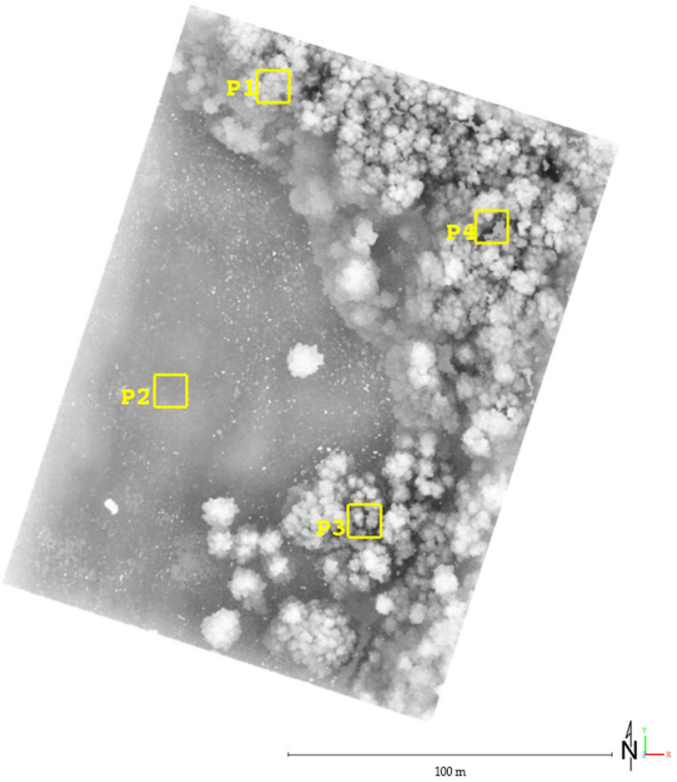

Figure 11. Selected polygons for detailed data analysis in the forested area. P1: High vegetation; P2: meadow; P3: low vegetation; P4: high vegetation with canopy gaps.

P1 (high vegetation) polygon covers an area with dense and high vegetation, representing mature trees and thick canopy layers. It is characterized by pronounced vertical vegetation profiles, making it suitable for evaluating the performance of point cloud data in complex canopy conditions. P2 (Meadow) polygon represents an open meadow area without a tree cover. It is ideal for assessing point density and accuracy in an unobstructed environment. P3 (Low vegetation) polygon captures an area with low vegetation, such as shrubs or young trees. The variable heights of the vegetation in this polygon make it a good test case for evaluating subcanopy penetration and point cloud accuracy. P4 (High vegetation with canopy gaps) polygon represents an area with tall vegetation but with visible gaps in the canopy. It simulates a scenario where direct sunlight reaches the forest floor, making it ideal for studying light penetration and solar radiation modeling.

Figures 12–15 compare point cloud data from TLS, ALS, and ULS for P1, P2, P3, and P4. The comparison is presented from both the top view and side view, providing a visual representation of how each scanning technology captures the vertical structure of the canopy.

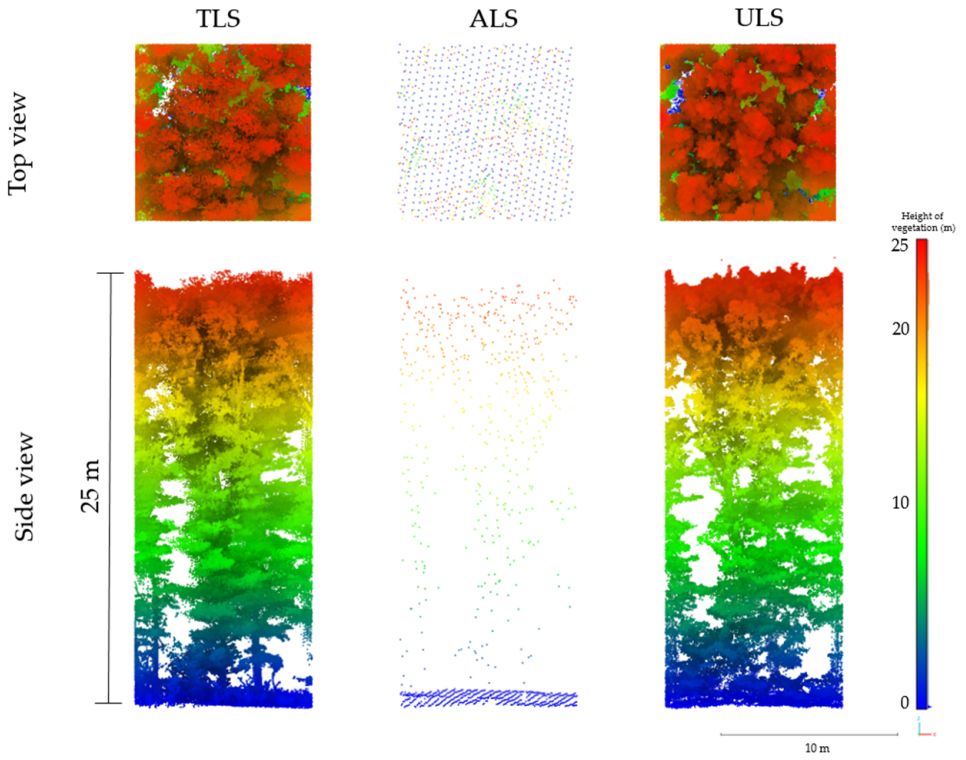

Figure 12. Comparison of TLS, ALS, and ULS data from the top and side views of polygon 1, 10 × 10 m, high vegetation.

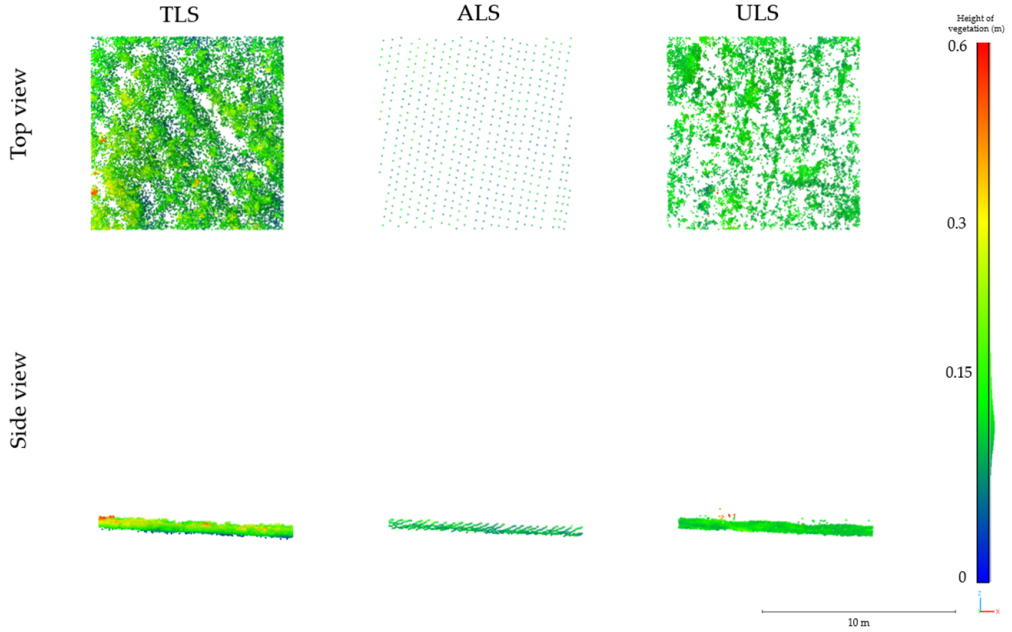

Figure 13. Comparison of TLS, ALS, and ULS data from the top and side views of polygon 2, 10 × 10 m, meadow.

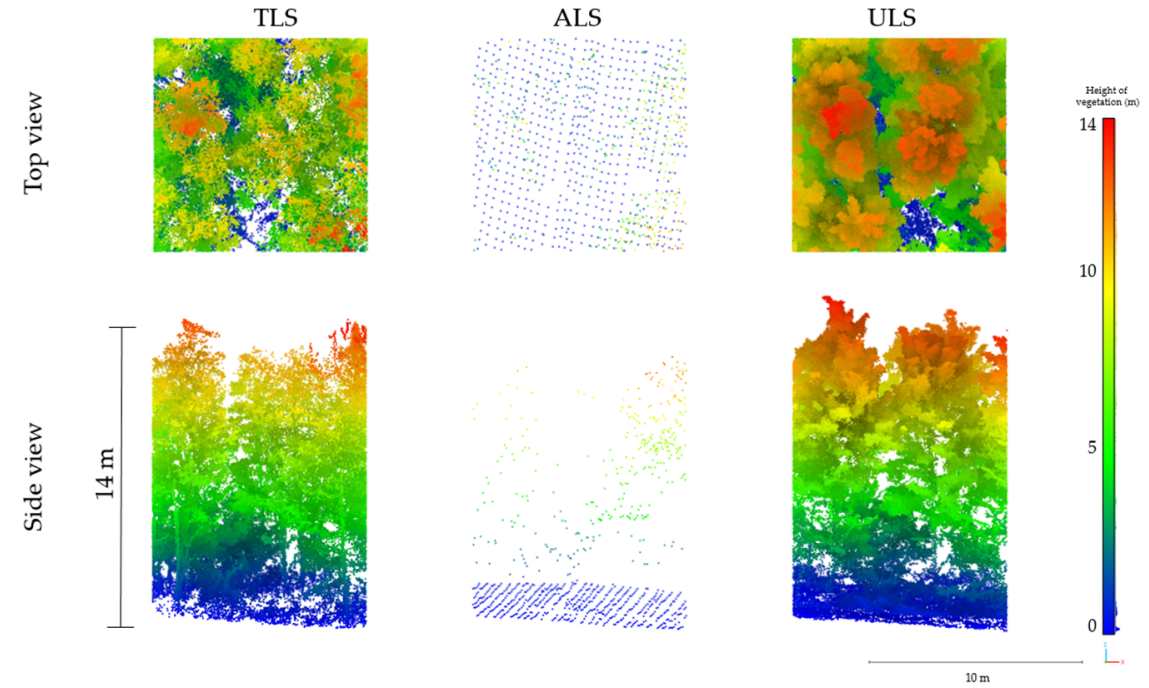

Figure 14. Comparison of TLS, ALS, and ULS data from the top and side views of polygon 3, 10 × 10 m, low vegetation.

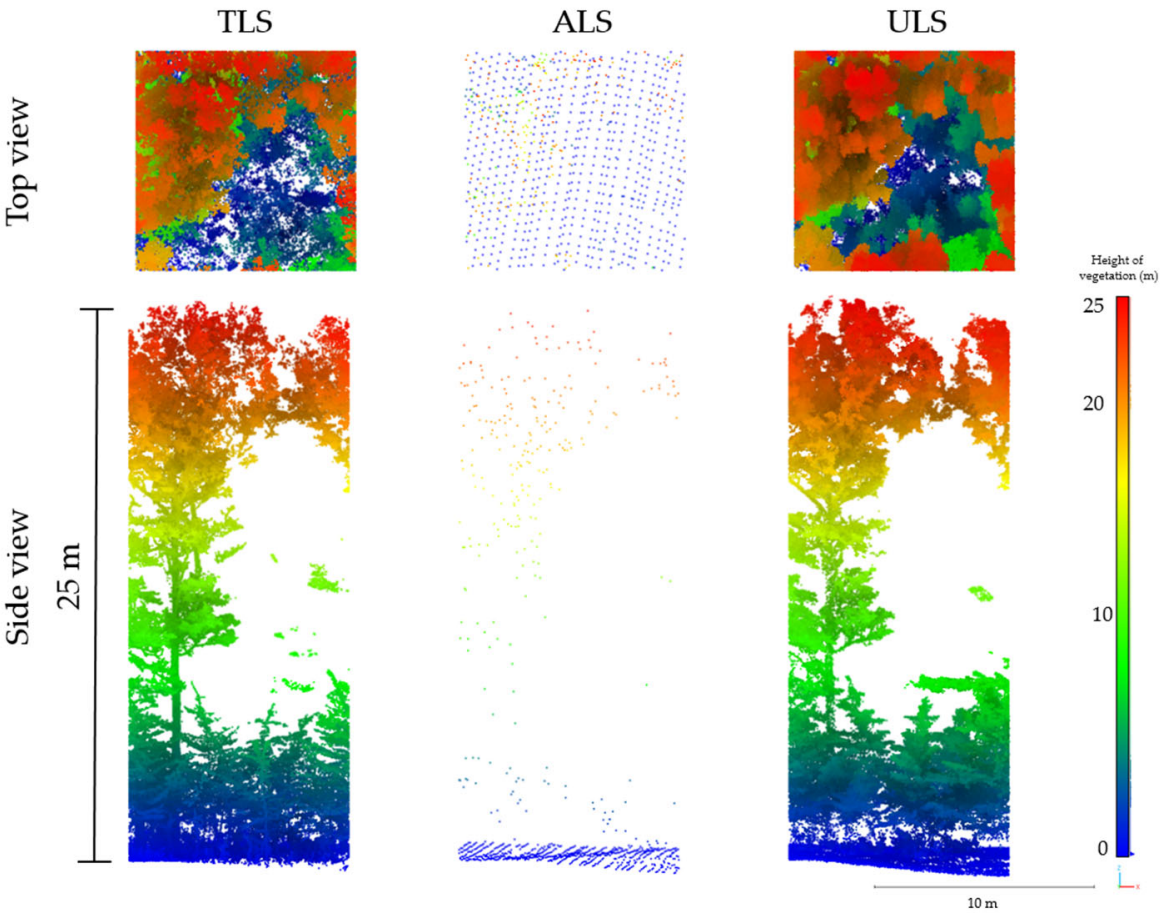

Figure 15. Comparison of TLS, ALS, and ULS data from the top and side views of polygon 4, 10 × 10 m, high vegetation with a gap in the vegetation.

In polygon 1 (Figure 12), TLS provides the highest density and detail in both the top and side views, capturing complex canopy structures and ground details. ALS has the sparsest point cloud, particularly in the side view, indicating that it captures limited detail in high and low vegetation layers. ULS offers a balance between ALS and TLS, providing more detail than ALS but slightly less than TLS in both views. This figure highlights the differences in point cloud density and vertical penetration among the three technologies, with TLS and ULS being more suitable for detailed forest structure analysis compared to ALS.

In the polygon 2 (Figure 13), TLS captures the most detailed point cloud data, providing a highly accurate representation of both the surface and vegetation structure of the meadow. ALS has the sparsest point cloud, limiting its ability to capture fine details of the meadow, which results in a less precise surface model. ULS offers an intermediate point density, capturing more detail than ALS but less than TLS. It provides a good balance between resolution and coverage for analyzing larger surface features.

The comparison of TLS, ALS, and ULS for low vegetation in polygon 3 (Figure 14) highlights significant differences in the ability of these technologies to capture detailed vegetation structure. Given the nature of low vegetation, which includes smaller plants, shrubs, and young trees, the level of detail and point density is critical for accurate analysis. For detailed analysis of low vegetation, TLS is the most reliable scanning method, offering high resolution and accuracy. ULS provides a reasonably detailed alternative for capturing low vegetation structure. Unlike TLS, however, ULS reaches its limits in this case when it comes to the detailed capture of tree trunks and the structure of small branches. ALS is not well suited for this task due to its sparse point cloud and inability to capture fine-scale vegetation details.

Figure 15 compares the capabilities of three LiDAR scanning methods—in capturing the structure of a 10 × 10 m plot of dense vegetation with a gap in the vegetation. TLS and ULS provide detailed and dense point clouds, both from the top and side views, accurately representing the vegetation's height and structure. ALS data are sparse and lack detail, especially in the side view, where it fails to capture lower vegetation and finer canopy details. The color gradient represents vegetation height, ranging from blue (low) to red (high). The comparison illustrates the superior resolution of TLS and ULS over ALS for capturing high-density vegetation.

Table 1 provides a comparison of different types of laser scanning data across four 10 × 10 m polygons (P1–P4) in the forested area (see Figure 11). The parameter height of vegetation indicates the maximum vegetation height present within each polygon. The canopy is further divided into two categories: canopy total, representing all points within the tree crown, and canopy top 5 m, representing the points located in the uppermost 5 m of the crown, where the largest concentration of biomass is typically found. For vegetation with a height of 25 m, TLS recorded the highest total number of points (418,463) and a density of 4184.63 points/m^2 followed by ULS with 2549.09 points/m^2, and a significantly lower density of 10.79 points/m^2 recorded by ALS. Data for P2 reflected a low-lying vegetated area. TLS recorded a point density of 252.78 points/m^2, ULS 94.15 points/m^2, and ALS 10.00 points/m^2. For this 14 m high vegetation (P3), TLS achieved a point density of 963.01 points/m^2 for the entire canopy, while ALS and ULS recorded 9.26 points/m^2 and 1932.72 points/m^2, respectively. TLS and ULS provided significantly higher detail, capturing lower vegetation layers and subcanopy points compared to ALS. Vegetation with a height of 25 m, TLS recorded 166,336 total points and a density of 1663.36 points/m^2 for the canopy, while ALS and ULS achieved densities of 8.77 points/m^2 and 1857.00 points/m^2, respectively (Table 1).

Table 1. Comparison of TLS, ALS, and ULS data in the selected polygons—forested area.

		TLS			ALS			ULS		
Height of Vegetation (m)	**Polygons 10 × 10 m**	**Points**	**%**	**Density**	**Points**	**%**	**Density**	**Points**	**%**	**Density**
25	P1 Total points	418,463	100	4184.63	1079	100	10.79	264,809	100	2648.09
	P1 Ground	17,830	4.26	178.3	557	51.62	5.57	9162	3.46	91.62
	P1 Canopy total	400,633	95.74	4006.33	522	48.38	5.22	255,647	96.54	2556.47
	P1 Canopy top 5 m	120,464	30.07	1204.64	246	47.13	2.46	113,384	44.35	1133.84
		Points	%	Density	Points	%	Density	Points	%	Density
0	P2 Total points	25,278	100	252.78	551	100	5.51	9415	100	94.15
	P2 Ground	-	-	-	-	-	-	-	-	-
	P2 Canopy total	-	-	-	-	-	-	-	-	-
	P2 Canopy top 5 m	-	-	-	-	-	-	-	-	-
		Points	%	Density	Points	%	Density	Points	%	Density
14	P3 Total points	96,301	100	963.01	926	100	9.26	193,272	100	1932.72
	P3 Ground	3269	3.39	32.69	573	61.88	5.73	9854	5.1	98.54
	P3 Canopy total	93,032	96.61	930.32	353	38.12	3.53	183,418	94.9	1834.18
	P3 Canopy top 5 m	11,759	12.64	117.59	95	26.91	0.95	83,387	45.46	833.87
		Points	%	Density	Points	%	Density	Points	%	Density
25	P4 Total points	164,336	100	1643.36	877	100	8.77	207,452	100	2074.52
	P4 Ground	10,712	6.52	107.12	600	68.42	6	124,88	6.02	124.52
	P4 Canopy total	153,624	93.48	1536.24	277	31.58	2.77	194,964	93.98	1949.64
	P4 Canopy top 5 m	31,565	20.55	315.65	102	36.82	1.02	61,025	31.3	610.25

The symbol "-" indicates that the calculation for the given statistic is not feasible.

TLS consistently provides the highest point density, capturing fine structural details of both ground and canopy layers. The main limitation of TLS is the significant fluctuation in point density. There is a high concentration of points near the scanner and at the forest edges, where trees are visible from multiple positions. In the case of the forest canopy, the higher the height, the lower the density of points. This means that the ground parts of the trees are captured best, but the canopy of the trees already reaches a lower density of points. ALS, with its lower point density, is suitable for the terrain and broader canopy outlines but lacks subcanopy detail. ULS offers a balance between coverage and detail, performing well in both dense and open canopy conditions. These metrics are crucial for selecting the appropriate scanning technology, depending on the specific analysis needs in forested environments, such as canopy structure assessment, ground surface modeling, or leaf point differentiation.

3.2. Point Clouds in the Built-Up Area

Figure 16 displays a view of a built-up area segmented into four distinct polygons (P1, P2, P3, and P4). These polygons have been selected for detailed data analysis using ALS and TLS datasets and represent different surface types and structures commonly found in an urban environment. The area includes buildings, vegetation, and open spaces. Each polygon is designated to capture specific features within the built-up landscape.

P1 (high vegetation) polygon is located in an area with tall trees. It is used to evaluate the ability of point cloud data to capture complex vertical structures, such as tree canopies. P2 (roof) polygon is positioned on the roof of a building. It is useful for analyzing flat, elevated surfaces and assessing the precision and density of the data. P3 (Parking lot) polygon is placed on a parking area with flat terrain. It serves to analyze the accuracy and density of point cloud data in capturing ground-level surfaces with no major obstructions. P4 (high vegetation) is similar to P1, this polygon is located in another area of high vegetation, allowing for comparative analysis of tree canopy structures and variations in point cloud representation across different vegetated regions.

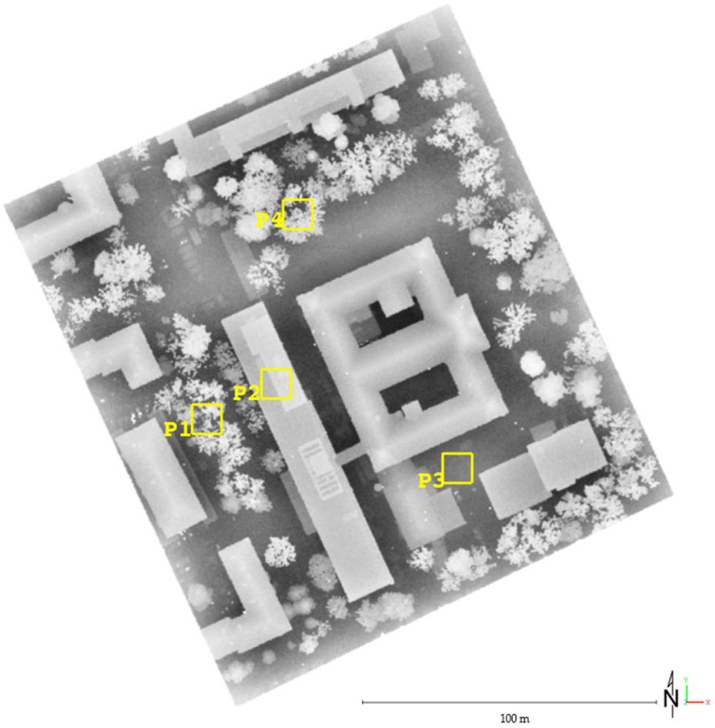

Figure 16. Selected polygons for detailed data analysis—built-up area. P1: high vegetation; P2: roof; P3: parking lot; P4: high vegetation.

Figures 17–20 compare point cloud data from TLS and ALS for P1, P2, P3, and P4. The comparison is presented from both the top view and side view, providing a visual representation of how each scanning technology captures the vertical structure of the canopy.

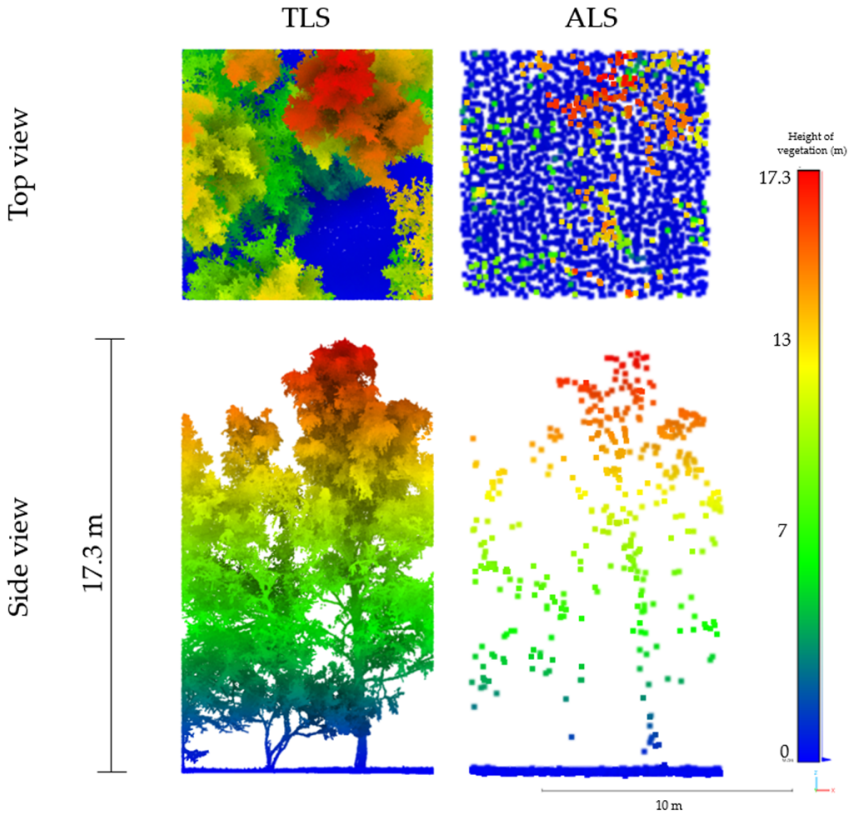

Figure 17. Comparison of TLS and ALS data from the top and side views of polygon 1, 10 × 10 m, high vegetation.

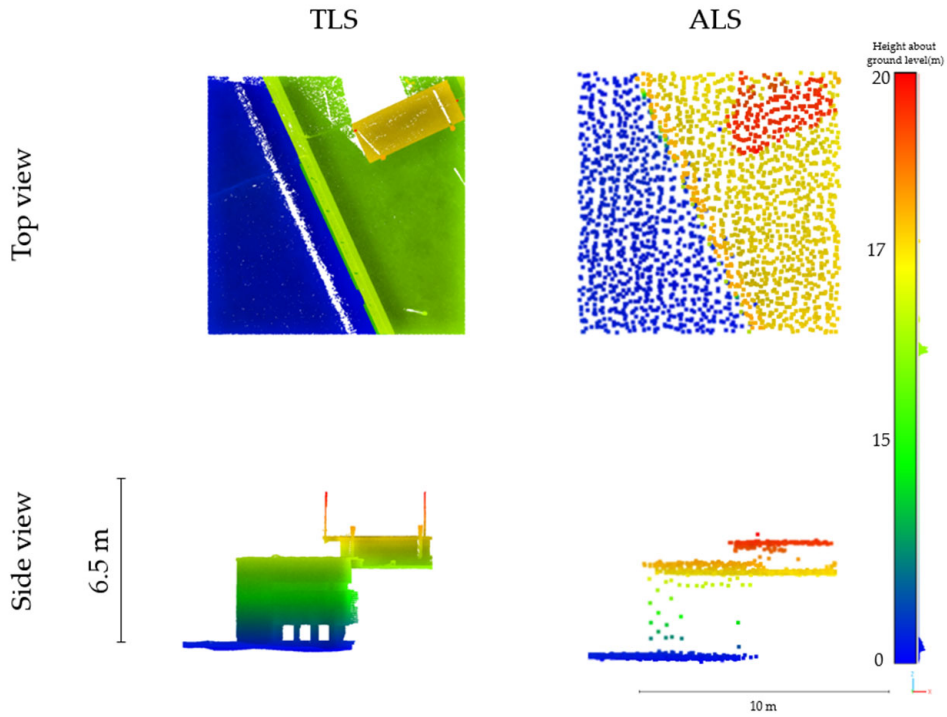

Figure 18. Comparison of TLS and ALS data from the top and side views of polygon 2, 10 × 10 m, roof.

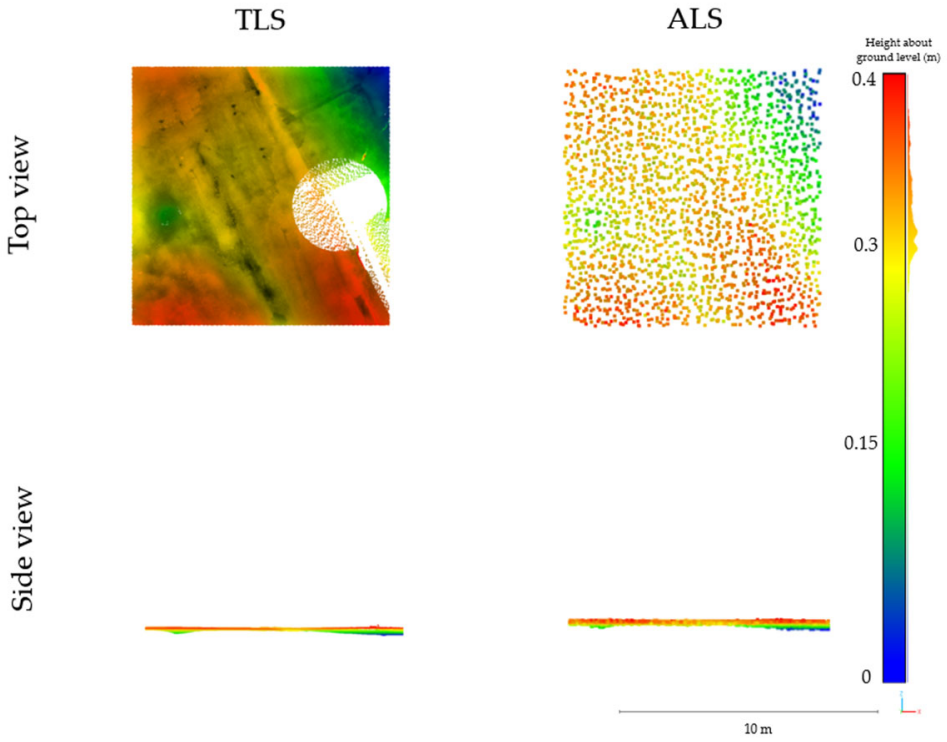

Figure 19. Comparison of TLS and ALS data from the top and side views of polygon 3, 10 × 10 m, parking.

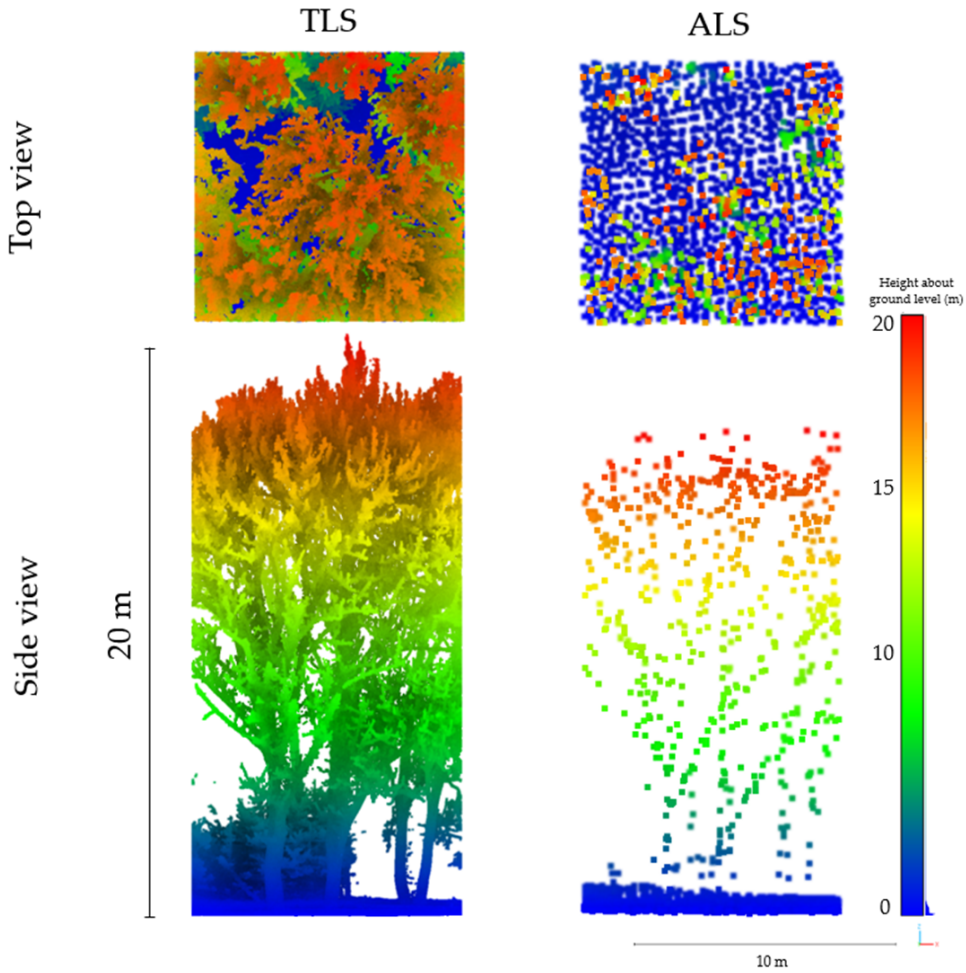

Figure 20. Comparison of TLS and ALS data from the top and side views of polygon 4, 10 × 10 m, high vegetation.

Figure 17 illustrates a comparison between ALS and TLS data for a 10 × 10 m area of high vegetation. TLS provides significantly higher resolution and detail in both top and side views compared to ALS. The top view from TLS captures intricate details of the tree canopy, while ALS data show a more generalized structure. In the side view, TLS highlights the detailed vertical structure of the tree, including lower branches, whereas ALS presents a less detailed vertical profile.

Figure 18 compares TLS and ALS data for a 10 × 10 m area with a roof structure. TLS provides significantly more detail and precision in both top and side views, capturing the roof's edges and small structural features more clearly. In contrast, ALS presents a coarser and less defined representation of the roof and its vertical profile.

Figure 19 compares TLS and ALS data for a 10 × 10 m parking lot area. TLS provides a much more detailed and accurate representation of the flat surface, both in the top and side views, capturing subtle elevation changes. ALS, on the other hand, offers a coarser resolution with fewer details, particularly in the side view. In the case of TLS data, we can observe the absence of data under the position of the scanner.

Figure 20 compares TLS and ALS data of a 10 × 10 m high vegetation from top and side views. TLS provides a denser, more detailed representation of the vegetation structure, while ALS shows a sparser point cloud with fewer details but captures the overall shape. TLS excels in precision, particularly in capturing fine details, whereas ALS offers a broader but less detailed overview.

Table 2 provides a comparison of TLS and ALS data across four 10 × 10 m polygons (P1–P4), focused on vegetation height and structure. TLS consistently captures significantly more points and provides much denser data compared to ALS across all polygons.

Table 2. Comparison of TLS and ALS data in the selected polygons—built-up area.

		TLS			ALS		
Height of Vegetation (m)	**Polygons 10 × 10 m**	**Points**	**%**	**Density**	**Points**	**%**	**Density**
17.3	P1 Total points	901,575	100	9015.75	2634	100	26.34
	P1 Ground	203,692	22.59	2036.92	2214	84.05	22.14
	P1 Canopy total	697,883	77.41	6978.83	420	15.95	4.2
	P1 Canopy top 5 m	262,281	37.58	2622.81	213	50.71	2.13
		Points	%	Density	Points	%	Density
0	P2 Total points	295,750	100	2957.50	2325	100	23.25
	P2 Ground	-	-	-	-	-	-
	P2 Canopy total	-	-	-	-	-	-
	P2 Canopy top 5 m	-	-	-	-	-	-
		Points	%	Density	Points	%	Density
0	P3 Total points	160,791	100	1607.91	2377	100	23.77
	P3 Ground	-	-	-	-	-	-
	P3 Canopy total	-	-	-	-	-	-
	P3 Canopy top 5 m	-	-	-	-	-	-
		Points	%	Density	Points	%	Density
20	P4 Total points	969,124	100	9691.24	2336	100	23.36
	P4 Ground	170,515	17.59	1705.15	1702	72.86	17.02
	P4 Canopy total	798,609	82.41	7986.09	634	27.14	6.34
	P4 Canopy top 5 m	273,612	34.26	2736.12	290	45.74	2.9

The symbol "-" indicates that the calculation for the given statistic is not feasible.

ALS data show a higher percentage of ground points, but a lower percentage and density of canopy points compared to TLS, especially in the higher vegetation polygons (P1 and P4). In P2 and P3, ALS and TLS both provide limited data, likely due to less or no vegetation in these areas. For canopy top (5 m) data, TLS captures a substantial number of points in P1 and P4, while ALS captures fewer points but with a higher percentage in P4.

3.3. Estimated Subcanopy Solar Radiation in the Forested Area

In this section, we present the estimation of subcanopy solar radiation in the forested area using the PCSRT model and the r.sun model implemented in GRASS GIS. To compare the performance and results of the models, four distinct small polygons (P1 to P4) within each study area were analyzed (Figure 11). The point cloud data collected through TLS, ULS, and ALS were processed and compared to evaluate the models' effectiveness. Furthermore, solar radiation attenuation was assessed using calculated polygons to better understand the spatial distribution of sunlight under varying canopy conditions.

Table 3 presents irradiance values (in W/m^2) for ground and canopy top across four polygons (P1 to P4). ULS and TLS provide more detailed and higher irradiance readings, with data for both ground and canopy top across all polygons.

Table 3. Average irradiance values calculated by PCSRT from ULS, TLS, and ALS data in W/m^2—forested area, 27 September 2023.

ULS		**P1**		**P2**		**P3**		**P4**
Time	**Ground**	**Canopy Top**	**Ground**	**Canopy Top**	**Ground**	**Canopy Top**	**Ground**	**Canopy Top**
8:00	61.11	199.04	446.93	-	56.67	169.71	61.78	185.41
10:00	140.72	399.27	655.34	-	226.54	395.46	146.48	412.50
12:00	460.30	447.13	699.37	-	198.49	431.95	162.12	435.48
14:00	372.81	456.45	672.27	-	218.19	456.04	190.19	444.29
16:00	189.79	315.38	530.98	-	154.46	323.63	140.71	302.14
TLS		P1		P2		P3		P4
Time	Ground	Canopy Top	Ground	Canopy Top	Ground	Canopy Top	Ground	Canopy Top
8:00	64.25	220.69	424.94	-	247.18	366.06	207.46	344.33
10:00	129.69	413.40	624.14	-	405.41	584.51	346.61	537.90
12:00	379.54	459.92	651.85	-	355.73	636.60	334.79	574.19
14:00	297.55	451.73	613.54	-	280.88	633.22	286.47	560.86
16:00	180.98	306.39	437.10	-	114.66	504.25	118.65	403.38
ALS		P1		P2		P3		P4
Time	Ground	Canopy Top	Ground	Canopy Top	Ground	Canopy Top	Ground	Canopy Top
8:00	92.18	294.99	408.92	-	74.77	193.07	125.30	326.43
10:00	243.05	534.64	704.90	-	413.48	401.35	279.15	558.47
12:00	707.24	623.36	756.09	-	427.31	486.81	333.67	544.20
14:00	642.97	615.07	717.20	-	528.03	599.84	388.93	638.48
16:00	465.78	474.54	572.35	-	410.26	577.03	300.10	494.77

The symbol "-" indicates that the calculation for the given statistic is not feasible.

ALS shows generally lower irradiance values. Ground irradiance values are fairly consistent across all methods, while canopy top values show greater variation, especially in ALS. This comparison highlights ULS and TLS as superior in capturing spatial detail and greatly affecting irradiance data in forested areas, while ALS provides less coverage and lower irradiance readings (see Figures 21–23).

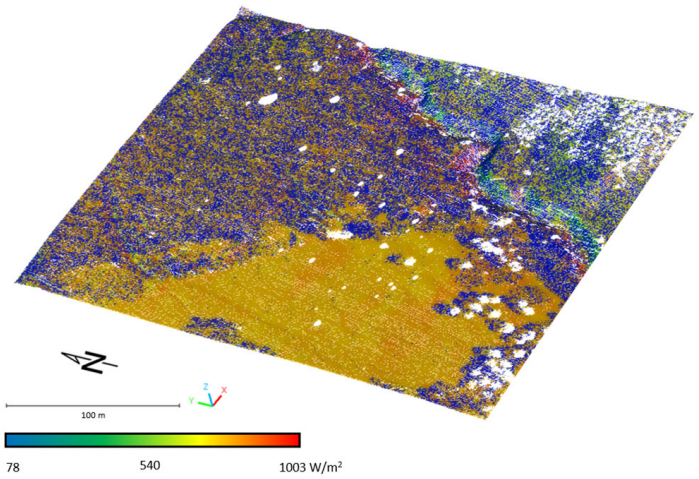

Figure 21. Estimated subcanopy solar radiation by PCSRT in forested area—ALS data; 27 September 2023, 12 a.m.

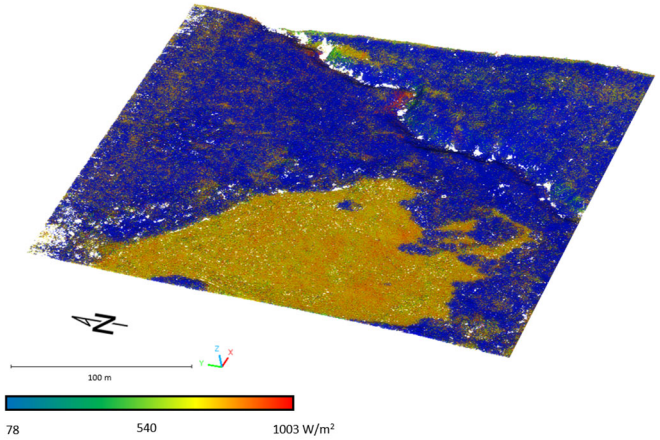

Figure 22. Estimated subcanopy solar radiation by PCSRT in forested area—ULS data; 27 September 2023, 12 a.m.

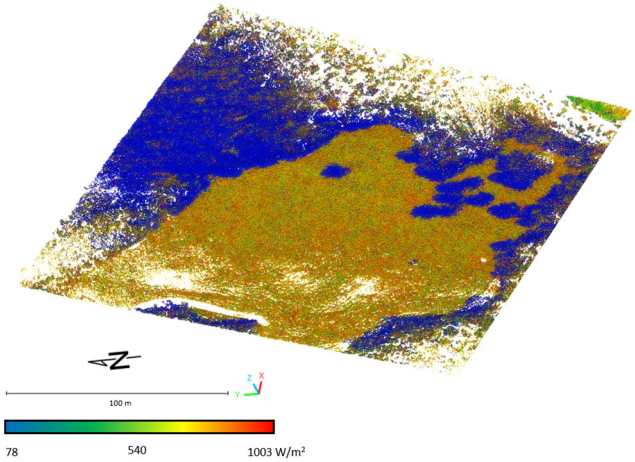

Figure 23. Estimated subcanopy solar radiation by PCSRT in forested area—TLS data; 27 September 2023, 12 a.m.

The estimation of subcanopy solar radiation was conducted in areas with the canopy layer (refer to Figure 1A). Figures 21–23 present the results of solar radiation modeling by PCSRT on the terrain beneath the tree canopy in the forested area on 27 September 2023, at 12 a.m. To enhance the visualization of solar radiation distribution, the point clouds representing the canopy were filtered out, revealing the underlying terrain. Figure 21 represents subcanopy solar radiation distribution using the ALS data. Due to the low density of points, the model reveals significant spatial variations in solar radiation within the forested area. We can also observe missing data directly under the crowns of some trees (white areas).

Figure 22 represents the estimated subcanopy solar radiation distribution using the ULS data. It indicates that the model was able to capture the variations in solar radiation due to factors such as tree canopy density, slope orientation, and other topographic features.

Figure 23 represents the estimated subcanopy solar radiation distribution using the TLS data. We can observe that the estimated subcanopy solar radiation is sufficiently modeled only in the areas where the scanning positions were located. Further outside of these positions, the white areas are present, indicating missing data.

Table 4 presents the comparison of solar radiation values captured by the pyranometers and modeled by the PCSRT for all data types, showing how closely the modeling corresponds to the actual measurements at various times of the day. Pyranometer readings generally increase throughout the day, peaking around noon to early afternoon, with

some drop-off towards late afternoon. ULS shows consistent readings that are generally close to pyranometer values, especially in the morning and midday. ALS tends to have higher readings than ULS and the pyranometer, particularly around 2:00 p.m. This is due to missing canopy data thus affecting sub-canopy solar radiation estimation. TLS data are only available for Pyranometer A and B at select times and align closely with ALS at those points.

Table 4. Validation measurements and solar irradiance in W/m^2 calculated by PCSRT, forested area, 28 September 2023 (for localization of pyranometers see Figure 9).

PYRANOMETER A				
TIME	**PYRANOMETER**	**ULS**	**ALS**	**TLS**
10:00:00	617.542	590.997	664.745	593.198
12:00:00	777.954	777.237	765.97	721.913
14:00:00	672.696	637.349	779.813	620.007
16:00:00	346.068	295.425	655.849	302.356
PYRANOMETER B				
TIME	PYRANOMETER	ULS	ALS	TLS
10:00:00	73.085	89.322	687.937	84.972
12:00:00	90.258	99.443	100.04	94.644
14:00:00	703.066	680.618	745.775	729.164
16:00:00	402.928	437.489	617.777	413.154
PYRANOMETER C				
TIME	PYRANOMETER	ULS	ALS	TLS
10:00:00	68.628	89.322	695.264	N/A
12:00:00	64.032	87.185	100.04	N/A
14:00:00	308.327	240.642	745.817	N/A
16:00:00	39.44	73.787	614.322	N/A
PYRANOMETER D				
TIME	PYRANOMETER	ULS	ALS	TLS
10:00:00	90.284	89.322	695.264	N/A
12:00:00	110.056	99.488	100.04	N/A
14:00:00	60.299	95.842	745.817	N/A
16:00:00	30.304	73.785	614.322	N/A

N/A—not available data.

For modeling solar radiation with the r.sun tool, we utilized data from three types of laser scanning ULS, TLS, and ALS. These data sources provide high-resolution, three-dimensional information on canopy structure, topography, and ground cover, which are critical for accurately simulating solar radiation in complex landscapes. The model was run on 27 September 2023, at 10:00 a.m. To account for atmospheric conditions, the Linke turbidity coefficient was set to 2.5, which represents a moderate level of atmospheric clarity based on seasonal averages. This parameter helps refine the model by accounting for the scattering and absorption of solar radiation due to atmospheric particles and gasses.

To simulate the attenuation of beam solar radiation by the tree canopy, we used the coeff_bh parameter in the r.sun module. The coeff_bh parameter was estimated using the LPI calculated individually from the ULS, TLS, and ALS-derived point clouds with a fine spatial resolution of 0.5 × 0.5 m. The spatial extent of the LPI calculation aligned with the canopy layer (see Figure 1). LPI was calculated by first identifying vegetation taller than 2 m within the point cloud, based on the distance between the vegetation and the terrain. For each 1 × 1 m window, the number of points was determined for both the full point cloud and the ground-only points (after vegetation removal). The LPI was then calculated as the ratio of ground points to total points. To account for spatial variability, the median

LPI values were aggregated to a coarser resolution of 3 × 3 m. These aggregated values were used to create the input raster layer for the coeff_bh parameter, allowing the model to represent the spatial heterogeneity of canopy density and structural complexity.

Figure 24 shows the solar irradiance calculated by the r.sun module using the ULS data for the ground under the canopy. The ULS data are a high-density point cloud enabling comprehensive and continuous coverage of tree surfaces within the study area. This high-resolution dataset captures the intricate details of the forest canopy, including the complex structure and variability of individual tree crowns. Such fine spatial resolution allows the r.sun model to accurately simulate the shading and light distribution patterns within the subcanopy environment. As a result of the detailed ULS data, the solar radiation estimation model produces reliable results, accurately reflecting the influence of canopy gaps, foliage density, and tree structure on subcanopy radiation levels. This dataset's ability to capture complex vegetation geometry ensures that areas with dense foliage display lower solar radiation values, while canopy gaps and less densely vegetated regions exhibit higher values.

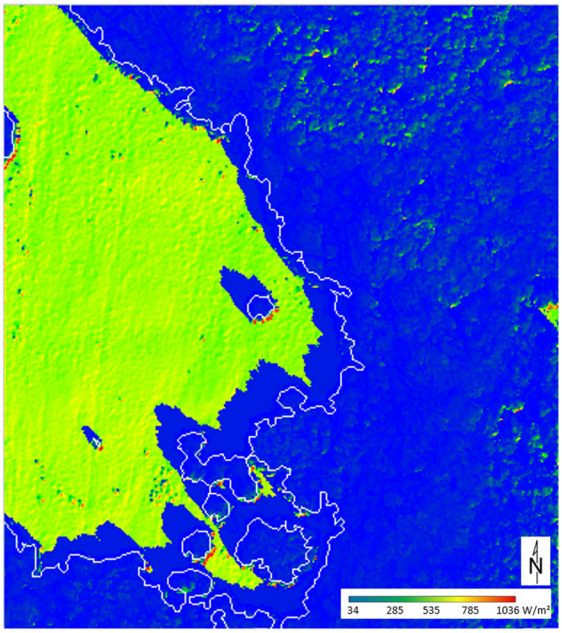

Figure 24. Estimated subcanopy solar radiation by r.sun—ULS data; 27 September 2023, 10 a.m.; white line—computing region for LPI.

Figure 25 shows the solar irradiance calculated by the r.sun module using the ALS data for the ground under the canopy. The results of solar radiation estimation using ALS data highlight limitations associated with the lower point density. In areas covered by vegetation, the model output reveals a high amount of solar radiation reaching the terrain, particularly in regions where shading from the canopy would be expected to reduce incident radiation significantly. This overestimation is due to the insufficient data resolution of ALS in capturing fine-scale canopy structures. This discrepancy suggests that, while ALS data are useful for broader canopy structure assessments, they may lack the detail necessary for accurate subcanopy radiation modeling in densely vegetated areas.

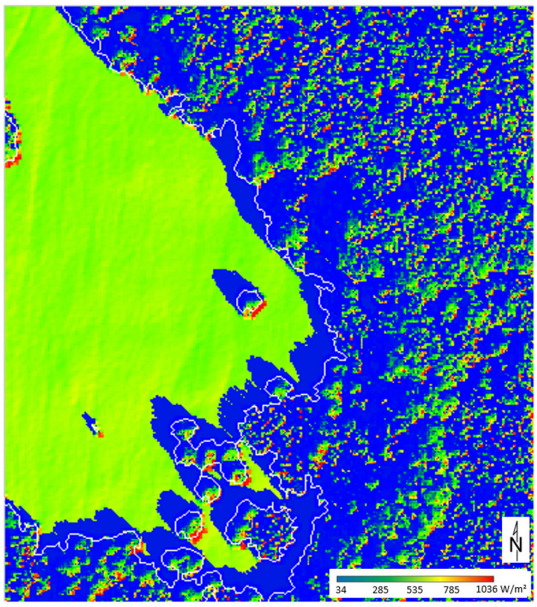

Figure 25. Estimated subcanopy solar radiation by r.sun—ALS data; 27 September 2023, 10 a.m.; white line—computing region for LPI.

Figure 26 shows the solar irradiance calculated by the r.sun module using the TLS data for the ground under the canopy. The density of point cloud data from TLS is sufficient for capturing detailed subcanopy features. However, the solar radiation estimates reveal certain limitations in representing the full structure of the upper canopy, particularly the crown surfaces. Since TLS is a ground-based method, it is inherently constrained in its ability to capture the topmost portions of tree crowns and higher canopy layers, often leading to gaps in the vertical structure of the canopy model. In densely vegetated areas, where one would expect substantial shading, there are regions with relatively high incident radiation, suggesting that the uppermost canopy layers may be incompletely represented. This effect can result in an overestimation of sunlight reaching the subcanopy, particularly in areas where TLS data cannot capture the complete height and spread of the tree crowns.

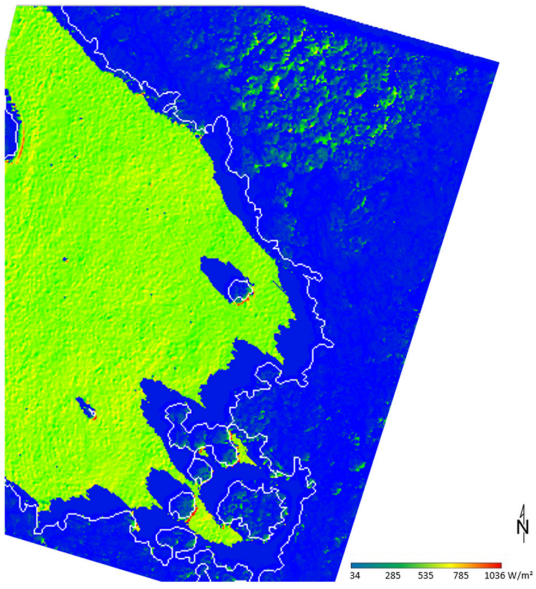

Figure 26. Estimated subcanopy solar radiation by r.sun—TLS data; 27 September 2023, 10 a.m.; white line—computing region for LPI.

Table 5 shows values of validation measurements and values from modeling using the r.sun module for forested areas. The differences between ULS, TLS, and ALS suggest that each data type has unique characteristics or assumptions impacting its irradiance estimates. The relatively close values of TLS to ULS imply that TLS may capture similar factors or environmental influences as ULS but with slightly lower values.

Table 5. Validation measurements and solar irradiance in W/m^2 calculated by r.sun, forested area, 27 September 2023 (for localization of pyranometers see Figure 9).

PYRANOMETER A				
TIME	**PYRANOMETER**	**ULS**	**ALS**	**TLS**
10:00:00	73.085	71.731	86.252	71.639
11:00:00	80.206	77.857	92.975	77.488
12:00:00	90.258	80.456	95.75	80.513
13:00:00	106.824	80.341	95.529	80.401
14:00:00	703.066	705.194	637.027	688.931
15:00:00	578.595	583.305	547.355	566.831
16:00:00	402.928	409.212	387.464	408.727
PYRANOMETER B				
TIME	PYRANOMETER	ULS	ALS	TLS
10:00:00	617.542	606.531	608.084	446.173
11:00:00	727.011	712.391	663.321	713.914
12:00:00	777.954	776.435	738.917	767.755
13:00:00	758.059	756.302	721.221	750.116
14:00:00	672.696	673.561	661.943	666.586
15:00:00	531.918	531.379	522.343	526.103
16:00:00	346.068	347.107	355.937	335.744
PYRANOMETER C				
TIME	PYRANOMETER	ULS	ALS	TLS
10:00:00	68.628	72.906	483.816	61.447
11:00:00	562.122	80.068	428.282	311.711
12:00:00	64.032	82.574	331.243	54.429
13:00:00	60.24	81.13	206.851	52.138
14:00:00	308.327	204.756	69.658	318.762
15:00:00	162.956	156.641	39.244	127.496
16:00:00	39.44	34.199	33.944	53.391
PYRANOMETER D				
TIME	PYRANOMETER	ULS	ALS	TLS
10:00:00	90.284	80.468	63.997	77.116
11:00:00	63.346	56.219	69.244	61.373
12:00:00	110.056	96.131	71.498	94.895
13:00:00	169.114	119.074	71.656	155.704
14:00:00	60.299	96.026	69.793	49.158
15:00:00	81.472	89.26	65.131	68.826
16:00:00	30.304	45.739	56.335	41.517

Significant differences can be seen in the case of pyranometers located in the forest (pyranometer C, D), especially with ALS data. Since the data were not dense enough in the vegetation area and the vegetation structure was not well captured, this was reflected between the measured and modeled values of the amount of solar radiation. Discrepancies between the measured and modeled values in the forested area may be attributed to the fact that data collection and pyranometer measurements were not conducted simultaneously. Given the geometric complexity and temporal variability of vegetation, changes in crown structure or slight movements of branches caused by wind could have occurred, potentially influencing the penetration of sunlight through the tree canopy.

3.4. Estimated Subcanopy Solar Radiation in the Built-Up Area

In this section, we present the estimation of subcanopy solar radiation in the built-up area using two models: the PCSRT model and the r.sun model implemented in GRASS GIS. To compare the performance and results of the two models, specific polygons within the built-up area were analyzed (Figure 16). The point cloud data collected through TLS and ALS were processed and compared to evaluate the models' effectiveness. Furthermore, solar radiation attenuation using r.sun was assessed using calculated LPI polygons to better understand the spatial distribution of sunlight under varying canopy conditions.

Table 6 presents a comparison of irradiance values (in W/m^2) between TLS and ALS data collected over the built-up area on 28 September 2023. The irradiance values are measured at different times of the day (8:00 a.m., 10:00 a.m., 12:00 a.m., 2:00 p.m., and 4:00 p.m.) for both ground and canopy top levels across four polygons (P1, P2, P3, and P4).

Table 6. Average irradiance values calculated by PCSRT for TLS and ALS data in W/m^2—built-up area, 28 September 2023.

TLS	**P1**		**P2**		**P3**		**P4**	
Time	**Ground**	**Canopy Top**	**Ground**	**Canopy Top**	**Ground**	**Canopy Top**	**Ground**	**Canopy Top**
8:00	93.85	164.00	221.51	-	221.51	-	169.63	238.13
10:00	93.85	164.00	221.51	-	96.92	-	169.63	238.13
12:00	305.11	282.77	539.63	-	672.70	-	478.26	432.93
14:00	209.98	288.51	640.19	-	610.30	-	274.75	468.72
16:00	193.68	231.67	504.62	-	265.00	-	207.30	371.06
ALS	P1		P2		P3		P4	
Time	Ground	Canopy Top	Ground	Canopy Top	Ground	Canopy Top	Ground	Canopy Top
8:00	326.68	438.03	391.33	-	204.58	-	299.95	400.96
10:00	498.08	538.37	513.21	-	429.97	-	582.67	517.61
12:00	0.86	0.92	0.99	-	0.97	-	0.94	0.97
14:00	0.63	0.95	0.99	-	0.89	-	0.92	0.94
16:00	0.85	0.94	0.95	-	0.39	-	0.85	0.97

The symbol "-" indicates that the calculation for the given statistic is not feasible.

Irradiance levels are generally higher for both ground and canopy in the morning (8:00 a.m. and 10:00 a.m.) and peak around midday (12:00 a.m.), with the afternoon (2:00 p.m. and 4:00 p.m.) showing a sharp decrease. TLS data show more consistent irradiance measurements throughout the day, whereas ALS data show significant variation, especially with much lower values recorded in the afternoon. Canopy top levels often receive higher irradiance than ground levels, especially during the morning hours, indicating higher exposure at elevated points. These data reflect the irradiance variation throughout the day for different measurement methods in a built-up area, highlighting the strengths of both TLS and ALS in different periods and terrain levels.

The estimation of solar radiation was conducted in all areas including areas with a canopy layer (refer to Figure 1B). Figures 27 and 28 present the results of solar radiation modeling on the terrain beneath the tree canopy in the built-up area. To enhance the visualization of solar radiation distribution, the point clouds representing the canopy were filtered out, revealing the underlying terrain.

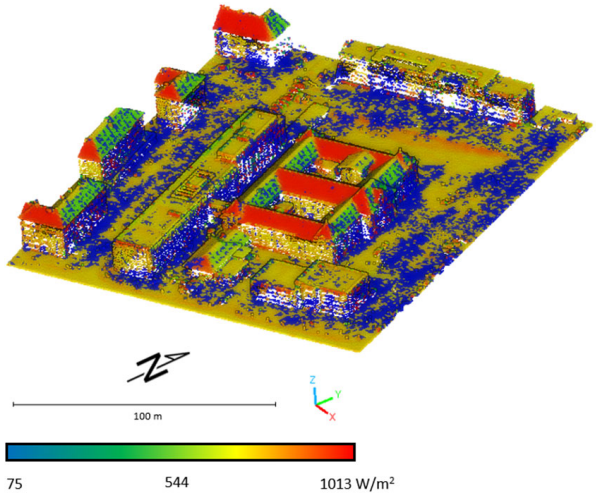

Figure 27. Estimated subcanopy solar radiation by PCSRT in built-up area—ALS data; 27 September 2023, 12 a.m.

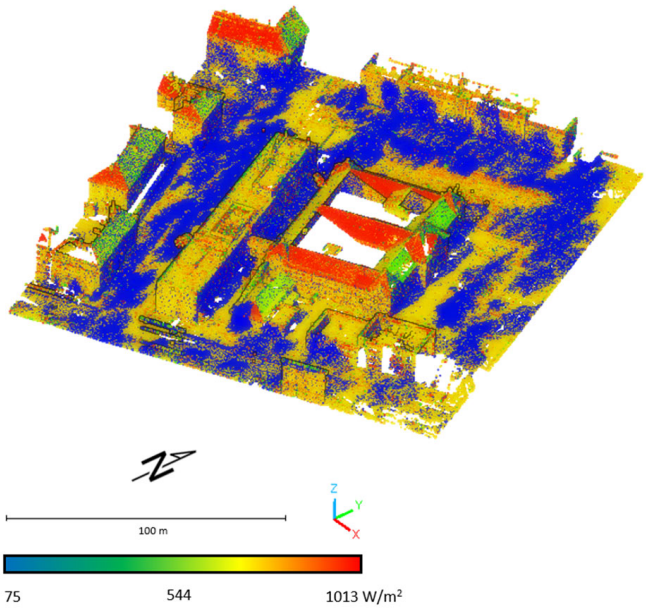

Figure 28. Estimated subcanopy solar radiation by PCSRT in built-up area—TLS data; 27 September 2023, 12 a.m.

Table 7 shows values of validation measurements and values from modeling using the PCSRT software for the built-up area. Some deviations exist between the measured values (from the pyranometer) and the modeled values (ALS and TLS data), which could be due to diffuse radiation, atmospheric conditions, or model inaccuracies.

Table 7. Values of validation measurements and values from modeling using the PCSRT model, built-up area, 28 September 2023 (for localization of the pyranometer see Figure 10).

PYRANOMETER A			
TIME	**PYRANOMETER**	**ALS**	**TLS**
10:00:00	533.578	615.933	490.058
12:00:00	670.942	653.664	703.752
14:00:00	581.518	652.778	626.85
16:00:00	309.94	568.497	559.602

For modeling solar radiation with the r.sun tool, we utilized the TLS and ALS data. The model was run on 28 September 2023, at 10:00 a.m. To account for atmospheric conditions, the Linke turbidity coefficient was set to 3, which represents a moderate level of atmospheric clarity based on seasonal averages. To simulate solar radiation attenuation within the study area, we incorporated an input raster layer representing the coeff_bh parameter.

LPI was calculated individually from the TLS, and ALS-derived point cloud with a fine spatial resolution of 0.5 × 0.5 m, and 1 × 1 m for ALS data, due to sparse vegetation data. The LPI calculation followed the same methodology as applied in the forested area. These aggregated values served as the input raster layer for the coeff_bh parameter. This parameter attenuates the beam component of solar radiation by estimating the influence of the canopy layer. The disadvantage is that it does not fully represent the 3D shape of the crown and thus we cannot obtain higher values of beam radiation under the highest crowns which start at a height of several meters, especially at low solar altitudes. The resulting values of the calculated global radiation by r.sun are, therefore, most accurate at high sun altitudes when the height of the crown does not have such a significant influence.

Figure 29 shows the estimated subcanopy solar radiation as modeled by the r.sun tool using the ALS data. The map captures the distribution of solar radiation in an urban area, accounting for the complex interactions of sunlight with both buildings and vegetation. Due to the sparse nature of ALS data, this map might not accurately represent solar radiation distribution in areas with dense canopy cover. In vegetated zones, the model may overestimate radiation by assuming sunlight reaches the ground in places where the canopy would realistically block it. This limitation affects the subcanopy analysis, as finer shading patterns and complex tree structures are not fully captured with ALS data. The results should be interpreted cautiously, especially in densely vegetated areas where ALS data's sparse resolution can lead to inaccuracies in subcanopy solar radiation estimates. For precise applications, such as evaluating solar access in heavily wooded areas or estimating microclimatic effects under tree cover, higher-density data sources, such as TLS, would offer better accuracy.

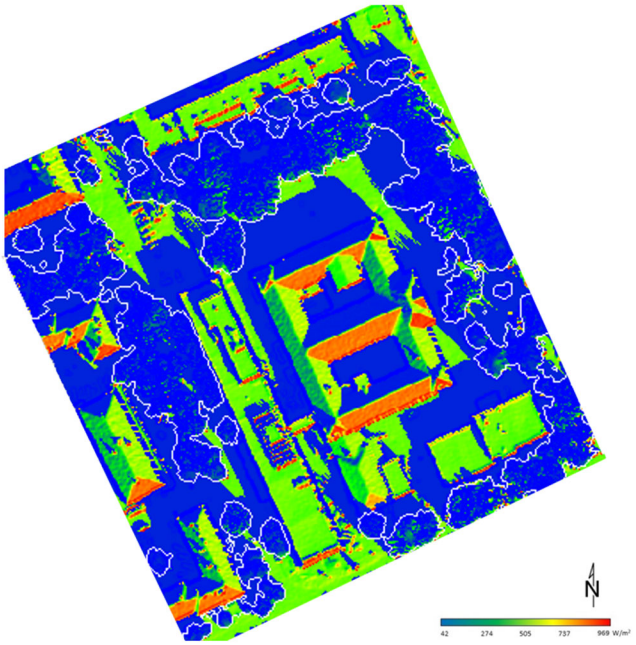

Figure 29. Estimated subcanopy solar radiation by r.sun—ALS data; 28 September 2023, 10 a.m.; white line—computing region for LPI.

Figure 30 represents the estimated subcanopy solar radiation calculated by the r.sun model using TLS data for the ground under the canopy. As in the case of the forested area, the limitations of TLS data are also evident in the built-up area. In certain sections, the TLS data do not fully capture the surfaces of building roofs or the tops of tree crowns. However, despite these limitations, the results are more detailed and accurate compared to those obtained from ALS data.

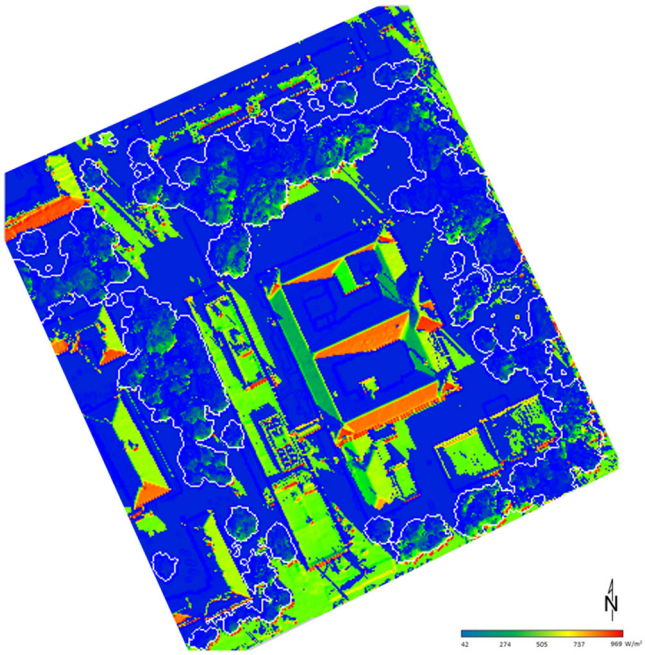

Figure 30. Estimated subcanopy solar radiation by r.sun—TLS data; 28 September 2023, 10 a.m.; white line—computing region for LPI.

The deviations in the validation between the solar radiation values that were modeled using r.sun and the values that were measured by the pyranometer (Table 8) can be explained by diffuse and reflected radiation since there is light-colored gravel on the roof where the pyranometer was placed. Also, deviations can arise due to atmospheric conditions and complex local environmental settings.

Table 8. Values of validation measurements and values from modeling using the r.sun module, built-up area, 28 September 2023 (for localization of pyranometers see Figure 10).

PYRANOMETER A			
TIME	**PYRANOMETER**	**ALS**	**TLS**
9:00:00	386.319	338.802	330.278
10:00:00	533.578	485.354	476.621
11:00:00	625.63	592.889	585.085
12:00:00	670.942	650.510	644.491
13:00:00	657.264	653.255	649.592
14:00:00	581.518	600.979	599.943
15:00:00	471.407	498.297	499.810
16:00:00	309.94	355.540	359.094

3.5. The Difference in Solar Radiation Estimates

This section investigates the discrepancies in subcanopy solar radiation estimates produced by two modeling tools, r.sun, and PCSRT, across both built-up and forested environments. By creating difference maps (Figures 31 and 32) that subtract the radiation rasters generated by each tool, this analysis highlights variations in their outputs, offering

a visual and quantitative perspective on model-specific biases and limitations. The comparison provides insights into how each tool performs across different land cover types, particularly in terms of their sensitivity to canopy structure and data resolution.

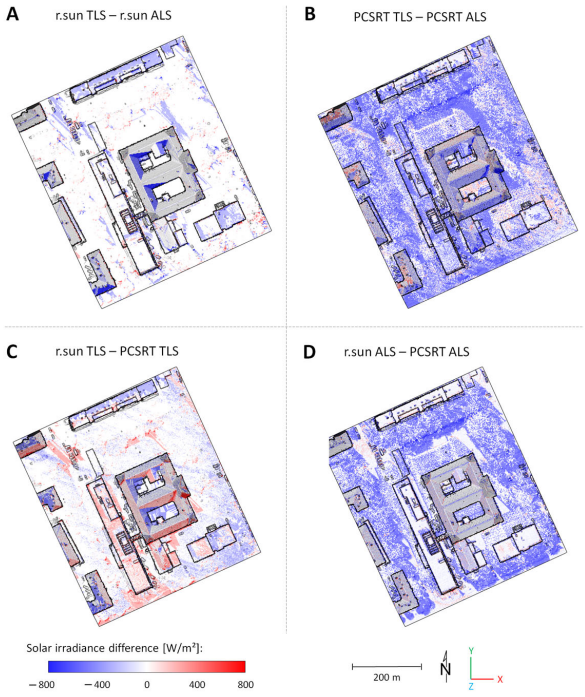

Figure 31. Solar irradiance difference maps between r.sun and PCSRT models using the TLS and ALS data, built-up area; (**A**): difference between r.sun TLS—r.sun ALS, (**B**): difference between PCSRT TLS—PCSRT ALS, (**C**): difference between r.sun TLS—PCSRT TLS, (**D**): difference between r.sun ALS—PCSRT ALS.

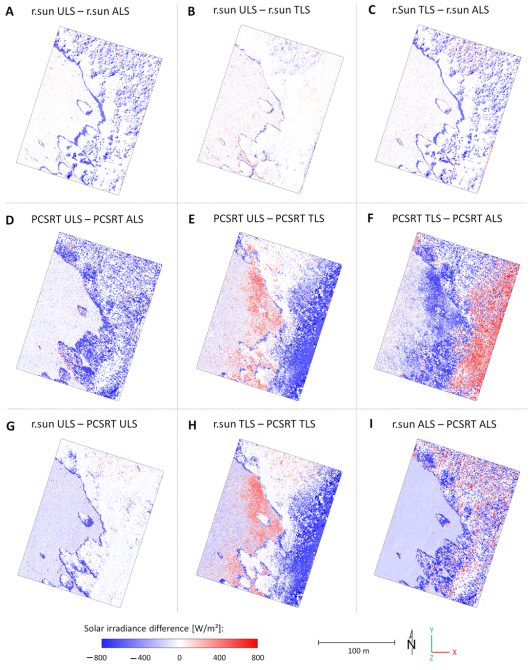

Figure 32. Solar irradiance difference maps between r.sun and PCSRT models—ULS, ALS, and TLS data, forested area; (**A**): difference between r.sun ULS—r.sun ALS, (**B**): difference between r.sun ULS—r.sun TLS, (**C**): difference between r.sun TLS—r.sun ALS, (**D**): difference between PCSRT ULS—PCSRT ALS, (**E**): PCSRT ULS—PCSRT TLS, (**F**): PCSRT TLS—PCSRT ALS, (**G**): r.sun ULS—PCSRT ULS, (**H**): r.sun TLS—PCSRT TLS, (**I**): r.sun ALS—PCSRT ALS.

To ensure a comprehensive evaluation, these analyses were conducted using all three data types: ULS, ALS, and TLS. Additionally, histograms (Figures 33 and 34) for each difference map were generated to quantify and statistically interpret the variations in subcanopy solar radiation estimates. These complementary visual and statistical analyses deepen the understanding of the factors influencing model performance and the inherent differences between raster- and voxel-based approaches under varying environmental and data conditions. Figure 31 illustrates the spatial differences in solar radiation estimates between two models—r.sun and PCSRT—in a built-up urban area, based on TLS and ALS data. White regions, where both models closely agree, are located in open areas (like roofs) and also areas with vegetation. Here, both models appear to handle sunlight distribution similarly. The blue regions show where the PCSRT model estimates higher solar radiation compared to the r.sun model. The red areas indicate zones where data coverage was insufficient.

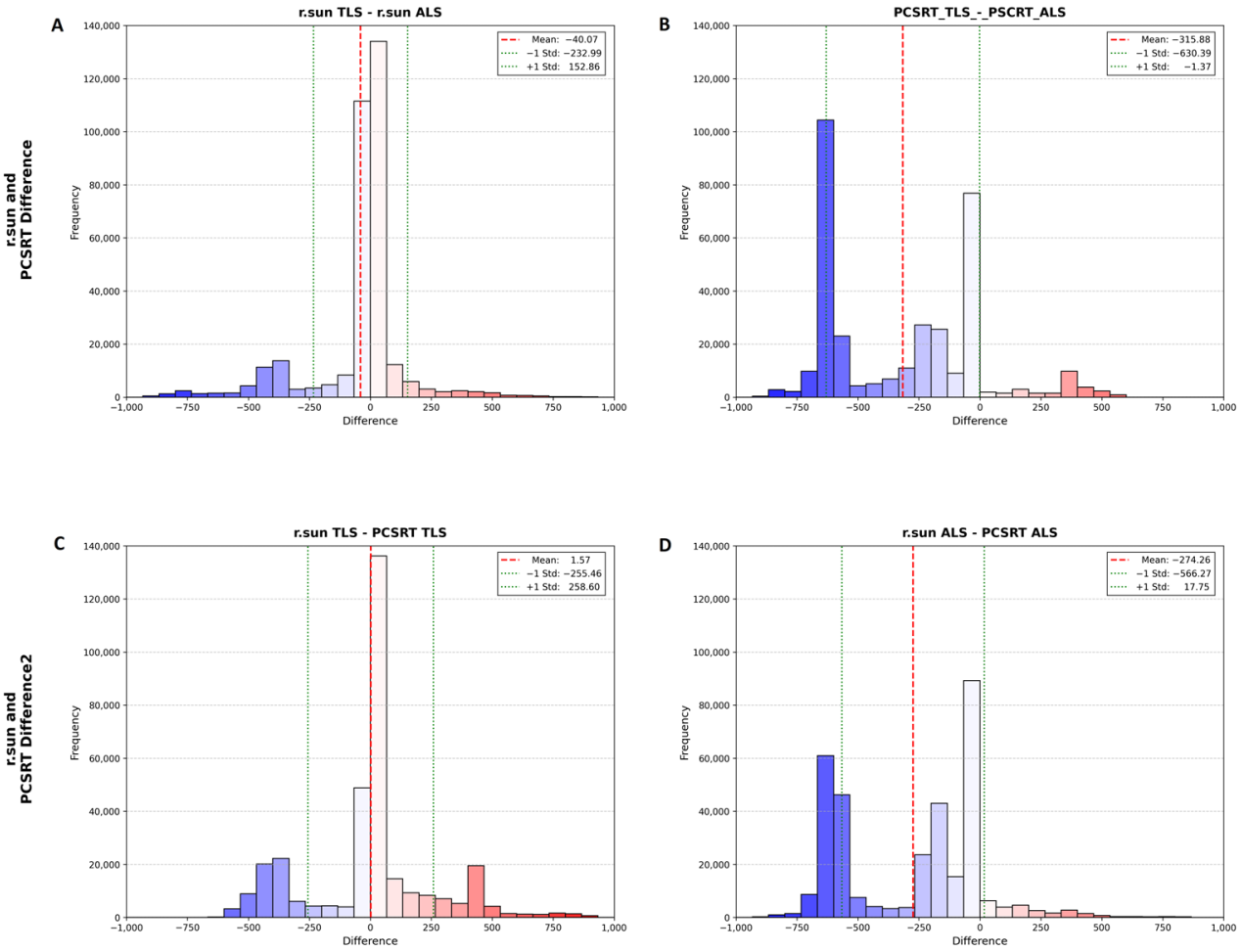

Figure 33. Solar irradiance difference histograms between r.sun and PCSRT models using the TLS and ALS data, built-up area; (**A**): difference between r.sun TLS—r.sun ALS, (**B**): difference between PCSRT TLS—PCSRT ALS, (**C**): difference between r.sun TLS—PCSRT TLS, (**D**): difference between r.sun ALS—PCSRT ALS.

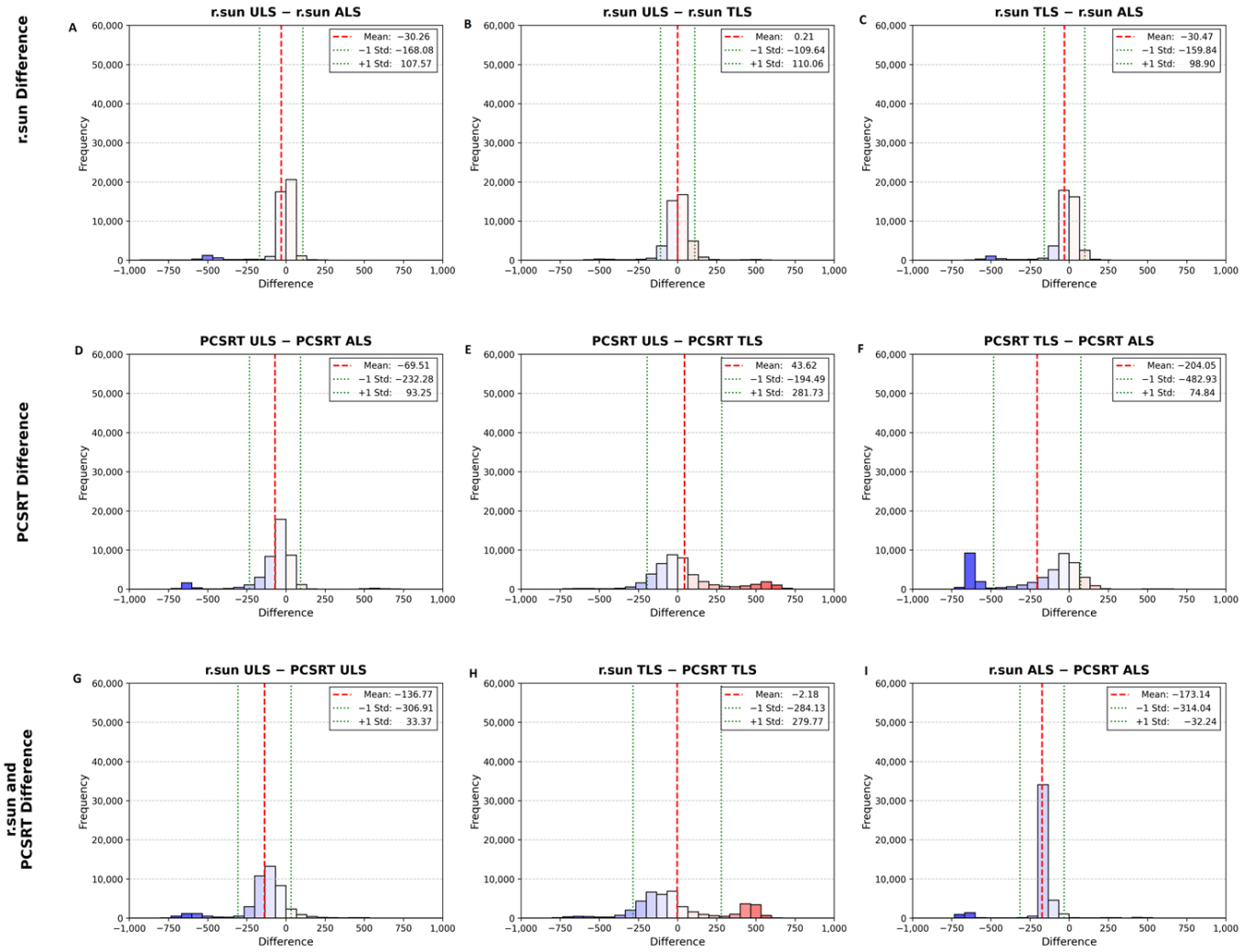

Figure 34. Solar irradiance histograms between r.sun and PCSRT models—ULS, ALS, and TLS data, forested area; (**A**): difference between r.sun ULS—r.sun ALS, (**B**): difference between r.sun ULS—r.sun TLS, (**C**): difference between r.sun TLS—r.sun ALS, (**D**): difference between PCSRT ULS—PCSRT ALS, (**E**): PCSRT ULS—PCSRT TLS, (**F**): PCSRT TLS—PCSRT ALS, (**G**): r.sun ULS—PCSRT ULS, (**H**): r.sun TLS—PCSRT TLS, (**I**): r.sun ALS—PCSRT ALS..

This limitation arises from the characteristics of the TLS method, which depends on an adequate number of strategically placed scanning positions to achieve comprehensive coverage. Due to its ground-based perspective, TLS is inherently restricted in its ability to capture certain parts of the canopy and upper structures, resulting in incomplete data in areas beyond its line of sight.

For ALS data, the differences between the models reflect the resolution and density of the point cloud. While ALS provides aerial coverage that overcomes some of the line-of-sight limitations of TLS, its relatively sparse data density compared to TLS can lead to the underrepresentation of finer structural details. This limitation affects the PCSRT model's ability to accurately represent shading and light attenuation in urban areas with dense or fragmented structures. Additionally, the reliance on ALS-derived DSMs for the r.sun model can further oversimplify the radiation modeling in such environments, contributing to the observed differences.

The histogram (Figure 33A–D) findings provide a quantitative basis for understanding the spatial patterns observed in the difference maps, offering insights into the limitations and capabilities of TLS and ALS data for solar radiation modeling in complex urban envi-

ronments. Histogram 32B demonstrates that the differences in solar radiation modeling between ALS and TLS data using the PCSRT model are substantial. These results highlight that ALS data, characterized by insufficient density to accurately capture the detailed structure of vegetation, lead to significant discrepancies when compared to TLS data, which provide high-resolution, precise representations of canopy structure. Histogram 32C illustrates that when sufficiently dense data, such as TLS, are employed, the differences between the r.sun and PCSRT models in estimating solar radiation are minimal. These results suggest that both models are capable of delivering reliable solar radiation estimates when provided with high-density input data that adequately represent the subcanopy environment. This observation highlights the importance of data resolution in ensuring the robustness and accuracy of solar radiation modeling across different computational approaches.

Figure 32 shows a map of the differences in solar radiation estimations between two different modeling approaches, r.sun, and PCSRT, using the ULS, ALS, and TLS data in the forest area. The difference maps reveal areas with minimal discrepancies (white regions), indicating that both models provide relatively similar estimates of solar radiation in these locations. Such consistency is observed in areas where structural complexity is low or uniform. Blue regions, where the PCSRT model estimates higher solar radiation compared to r.sun, reflect the PCSRT model's ability to account for sunlight penetration beneath tree canopies, especially at lower solar angles. This difference highlights the advantage of PCSRT's 3D voxel-based approach over r.sun's 2D raster-based simulation, which does not capture subcanopy dynamics effectively.

Conversely, red regions correspond to open areas or locations with sparse canopy coverage, where sunlight penetration is less obstructed. Here, PCSRT often calculates higher solar radiation values due to its finer representation of canopy interactions. When comparing ALS data with ULS or TLS data, the PCSRT model tends to overestimate subcanopy solar radiation values. This overestimation stems from the insufficient density of ALS point cloud data, which fails to capture detailed canopy structures. In contrast, TLS data, while providing high-resolution point clouds, can introduce inaccuracies in areas with data noise or incomplete terrain coverage, leading to localized deviations in the modeled outputs.

The r.sun model, on the other hand, produces consistent subcanopy solar radiation estimates when applied with either TLS or ULS data (Figure 34B). This consistency underscores its reliance on 2D DSMs, which smooth out variations in input data resolution. However, the limitations of the r.sun model become apparent in regions with dense or complex canopy structures, where it fails to capture the finer-scale shading and light attenuation effects that PCSRT models effectively.

3.6. The Effect of Point Cloud Density on Model Performance

Point cloud density plays a critical role in the accuracy of solar radiation modeling, as it directly influences the level of structural detail captured in canopy representations. High-density point clouds, such as those from TLS and ULS, allow models like PCSRT to accurately voxelize complex canopy structures, capturing fine-scale shading effects and light attenuation. The TLS dataset had an average density of 1353.44 points/m^2 in the forested area and 3991.41 points/m^2 in the built-up area, providing high-resolution data for precise subcanopy solar radiation modeling. The ULS dataset, with an even higher density of 2559.85 points/m^2 in the forested area, contributed to even more accurate radiation predictions in forest study area. In contrast, lower-density ALS point clouds, with an average density of 20.38 points/m^2 in the forested area and 23.08 points/m^2 in the built-up area, offer broader coverage but lack the detail necessary for precise voxelization. While suitable for large-scale modeling, this lower resolution leads to oversimplifications in

shading and light transmission, especially in dense forest environments. The raster-based r.sun model is less directly sensitive to point cloud density, as it uses DSMs derived from the point clouds. However, the resolution of the DSM still affects the model's ability to capture fine-scale terrain and canopy variations. These findings highlight the trade-offs between scanning methods: dense point clouds provide higher accuracy but require more computational resources, while sparser datasets offer greater efficiency and scalability at the expense of detail.

3.7. The Comparative Analysis of Solar Radiation Modeling Tools

The PCSRT and r.sun models represent two distinct approaches to modeling solar radiation. PCSRT utilizes voxelized 3D point clouds to model solar radiation dynamics, offering fine-scale accuracy particularly suited for complex environments such as dense forests. In contrast, r.sun operates on 2D raster-based DSMs and is optimized for computational efficiency, making it ideal for large-scale applications.

PCSRT excels in environments with heterogeneous canopy structures, such as dense forests, by capturing detailed shading and light attenuation effects. Leverages high-density point clouds from LiDAR data, enabling precise modeling of subcanopy solar radiation. Flexible for high-resolution studies, particularly when used with TLS or ULS data. The PCSRT, while highly effective in modeling solar radiation in complex environments, has notable limitations. It is computationally intensive, requiring significant memory and processing power, which restricts its scalability for large regions. Additionally, the tool's accuracy heavily depends on the resolution and density of the input point clouds; sparse datasets, such as those from ALS, can result in modeling inaccuracies. Furthermore, PCSRT struggles in environments characterized by rapid temporal variability, such as areas with frequent cloud cover or dynamically changing canopy structures, where the temporal resolution of input data may not adequately capture these fluctuations.

The r.sun tool is highly efficient for large-scale studies, offering low computational demands and reliable performance in relatively simple terrains or urban areas with limited vegetation, where 2D DSMs provide sufficient accuracy for radiation modeling. It delivers consistent results under clear-sky conditions and uniform atmospheric parameters. However, the tool has limitations, particularly in capturing fine-scale subcanopy dynamics in dense or complex vegetation structures. Its reliance on raster-based data assumes homogeneity within cells, which can lead to oversimplifications in areas with steep topography or fragmented canopies. Additionally, its performance is constrained by the resolution of DSM inputs, often underestimating shading effects and light attenuation in detailed or heterogeneous environments.

Table 9 presents a comparative overview of the r.sun and PCSRT solar radiation modeling tools, focusing on key aspects such as data structure, input requirements, precision, validation results, computation time, and recommended applications. The r.sun model utilizes raster-based data and is better suited for broad-scale studies with computational constraints, offering faster computation times but moderate accuracy in forested environments. Conversely, PCSRT employs voxel-based point cloud data, achieving higher precision in capturing 3D canopy structures, particularly in heterogeneous environments, at the cost of increased computational demands. The observations highlight trade-offs between efficiency and detail, providing guidance for selecting the appropriate model based on study objectives.

Table 9. Key differences and observations between r.sun and PCSRT models.

Aspect	r.sun	PCSRT	Observations
Model data structure	Raster based	Voxel based	PCSRT has higher computational and memory demands
Input requirements	DSM, slope and aspect rasters	Processed and optimized point cloud	PCSRT is faster for data preparation
Precision in forested areas	Moderate accuracy, limited by 2D representation	High precision with 3D representation	PCSRT better captures subcanopy dynamics in dense forests
Precision in urban areas	Effective for simpler canopy structures	Effective for detailed canopy interactions	Both models perform well but differ based on structural complexity
Validation results	Aligns well with pyranometer readings, with slight underestimations in forests	Closely matches pyranometer readings with high accuracy	ULS data aligns well for both models, ALS less so in complex areas
Computation time	Faster (e.g., 5 s for a forested area)	Slower (e.g., 6 min for a forested area)	r.sun is better for large-scale applications, PCSRT for detailed studies
Recommended applications	Broad-scale studies with computational constraints	Fine-scale studies in heterogeneous environments	Trade-off between efficiency and detail

The choice of model should be guided by the study's objectives and environmental context. PCSRT is recommended for localized studies requiring high precision, especially in areas with complex canopy or terrain structures. r.sun, on the other hand, is more suitable for large-scale or regional applications where computational efficiency is critical.

4. Discussion

The comparison between the 2D, raster-based r.sun model and the 3D, voxel-based PCSRT model in estimating subcanopy solar radiation underlines the strengths and limitations of each approach. The results from the forested and urban landscapes reveal that the choice of input data significantly influences the model outcomes. PCSRT demonstrates significant advantages in environments characterized by complex canopy structures, such as dense forests. Its utilization of 3D voxelized point clouds enables detailed modeling of shadowing effects and solar radiation dynamics at a fine spatial scale. PCSRT performs optimally with data acquired from TLS or ULS, which provide high-density point clouds and detailed representations of canopy structures. Furthermore, PCSRT is adaptable to input data from various LiDAR sources, making it particularly suitable for small-scale studies requiring high precision. However, its applicability to large-scale studies is constrained by high memory and computational demands. Additionally, the accuracy of PCSRT is highly dependent on the resolution and density of the input point cloud, which may vary across different LiDAR acquisition methods.

The comparison of PCSRT and r.sun also revealed significant differences in their performance, particularly under complex terrain conditions. PCSRT, with its voxel-based approach, demonstrated superior accuracy in capturing subcanopy solar radiation dynamics, especially in forested areas with dense and heterogeneous canopy structures. This accuracy, however, comes at the cost of higher computational demands. For instance, processing TLS data for a forested area requires approximately 6 min and 23 GB of memory, reflecting the increased complexity of voxelizing high-density point clouds. Additionally, PCSRT's sensitivity to input parameters, such as voxel size and point cloud density, further emphasizes the need for careful parameter selection; smaller voxel sizes increase detail but significantly impact computation time and resource requirements.

In contrast, the r.sun model was designed to address the requirements of large-scale or regional studies, prioritizing computational efficiency and simpler data structures. Utilizing a raster-based approach, r.sun completed the same forested area in just 5 s,

with minimal memory usage. This computational efficiency highlights its suitability for large-scale studies and simpler terrains. However, its reliance on raster DSMs limits its ability to accurately simulate fine-scale shading effects and subcanopy light penetration in heterogeneous environments, such as dense forest canopies. Furthermore, r.sun's accuracy is influenced by raster resolution, with coarser DSMs failing to capture intricate variations in canopy and terrain.

The study also emphasizes the importance of point cloud data quality and resolution in determining modeling effectiveness. ULS, due to its high-resolution and detailed data capture, provides the most accurate solar radiation estimates, closely matching the ground-based pyranometer measurements. TLS, while offering precise local data, is limited by its small coverage area and not homogenous point cloud density and logistical challenges in data acquisition. ALS, despite its broader coverage, produces lower accuracies due to insufficient point density, particularly in complex forest structures. These findings suggest that while ALS is suitable for large-scale applications, ULS is preferable for detailed studies of forest light environments. Furthermore, integrating multiple data sources can potentially improve model reliability, as each method compensates for the limitations of the others.

The findings of this study underscore several potential avenues for future research to overcome the identified limitations. One promising direction is the development of hybrid approaches that combine the strengths of PCSRT and r.sun. Such approaches could leverage PCSRT's accuracy for critical areas requiring fine-scale precision while utilizing r.sun's computational efficiency for broader analyses. This integration could offer a balanced solution, accommodating diverse environmental conditions and study scales. Furthermore, enhancing both models could significantly improve their applicability. For PCSRT, implementing computational optimizations, such as more efficient algorithms and advanced preprocessing tools, could reduce memory and processing requirements, thereby expanding its usability in larger-scale studies. On the other hand, incorporating the ability to model vertical structures and 3D elements into r.sun could enhance its accuracy in complex forested environments, addressing some of the limitations associated with its reliance on 2D raster data.

Another crucial area for future research is refining the integration of TLS, ULS, and ALS data. Developing hybrid models that utilize the strengths of each data acquisition method could lead to improved simulations of subcanopy solar radiation across diverse landscapes. Additionally, refining PCSRT to handle varying voxel resolutions could enhance its adaptability in heterogeneous environments, particularly in landscapes with intricate canopy structures.

Expanding the scope of validation frameworks would further strengthen the robustness of these models. Increasing the density of pyranometer measurements and integrating additional data sources, such as satellite-derived solar radiation or UAV-based light sensors, could provide a more comprehensive basis for evaluating model performance. Furthermore, to enhance the generalizability of the findings, future studies should include a broader range of environmental conditions. These could encompass other forest types, such as coniferous-dominated stands, boreal forests, and Mediterranean woodlands, as well as urban configurations that range from densely populated megacities to low-density suburban areas with diverse vegetation compositions.

This study contributes valuable insights into the trade-offs between precision and efficiency in solar radiation modeling, providing guidance for selecting tools based on study objectives, environmental complexity, and resource constraints. By addressing the proposed recommendations, future work can enhance the accuracy and applicability of these models, offering more robust solutions for ecological and environmental research.

5. Conclusions

This study evaluated two solar radiation modeling approaches—PCSRT and r.sun—using data from TLS, ULS, and ALS, making several novel contributions to the field of solar radiation modeling. It addresses a research gap by employing GIS-based tools to estimate solar radiation beneath tree crowns—an approach not previously utilized in this context. Additionally, it introduces the innovative use of the r.sun tool, incorporating the real-sky coefficient derived from LPI as an input parameter for solar radiation attenuation caused by a canopy layer. This study also offers a new perspective on modeling subcanopy solar radiation using LiDAR data from various sources, emphasizing the importance of spatial variability in point clouds representing the canopy.

The results demonstrate that the choice of modeling tool and input data significantly affects solar radiation estimates, especially in complex environments. The PCSRT model, leveraging high-density point cloud data, provided superior accuracy in capturing subcanopy radiation dynamics, particularly in complex forest structures. In contrast, the raster-based r.sun model excelled in computational efficiency and scalability, making it more suitable for broader regional applications and simpler urban environments.

A key finding is the substantial influence of LiDAR data type and quality on modeling outcomes. ULS provided the most reliable results due to its high spatial resolution, closely matching ground-based pyranometer measurements. TLS captured highly detailed local data but faced challenges in spatial coverage and uniformity. ALS, despite offering broader coverage, exhibited the highest deviations, limiting its precision in intricate canopy environments and demonstrating its suitability primarily for large-scale assessments.

The findings also highlight practical implications. PCSRT is recommended for detailed, small-scale analyses requiring high precision, such as ecological modeling and silvicultural planning, while r.sun is ideal for large-scale applications where computational efficiency is paramount. These insights underscore the critical role of data acquisition methods and modeling tools in enhancing subcanopy solar radiation estimation, providing a methodological foundation for ecological modeling, forest management, and environmental planning practices.

However, the results of this study have some limitations. PCSRT's high computational demands restrict its application to smaller areas, while r.sun's reliance on raster DSMs limits its precision in heterogeneous landscapes. Therefore, future research should explore hybrid modeling frameworks that integrate the strengths of both models, optimizing precision and efficiency for diverse environmental conditions. Further validation across different vegetation types and varied atmospheric conditions would enhance the generalizability of these findings.

Author Contributions: Conceptualization, D.B. and J.H.; methodology, D.B., J.H., J.Š., and J.K.; software, D.B. and J.Š.; validation, D.B.; formal analysis, J.H. and J.K.; investigation, D.B. and J.K.; resources, D.B. and J.K.; data curation, D.B., J.Š., and J.K.; writing—original draft preparation, D.B., J.Š. and J.H.; writing—review and editing, D.B. and J.H.; visualization, D.B. and J.Š.; supervision, J.H.; project administration, J.H.; funding acquisition, J.H. All authors have read and agreed to the published version of the manuscript.

Funding: This research was funded by the Slovak Research and Development Agency (APVV) under the contract No. APVV-23-0210, by the Scientific Grant Agency of the Ministry of Education, Science, Research and Sport of the Slovak Republic and the Slovak Academy of Sciences (VEGA) under the contract No. 1/0085/23 and No. 1/0780/24, and by the VVGS Grant Application PF Research for years 2024–2025 under the contract No. vvgs-2024-3065.

Data Availability Statement: The data presented in this study are available on request from the corresponding author. The data are not publicly available due to privacy reasons.

Conflicts of Interest: The author declares no conflicts of interest. The funders had no role in the design of the study; in the collection, analyses, or interpretation of data; in the writing of the manuscript, or in the decision to publish the results.

References

1. Jennings, S.B.; Brown, A.G.; Sheil, D. Assessing forest canopies and understorey illumination: Canopy closure, canopy cover and other measures. *Forestry* **1999**, *72*, 59–74. [CrossRef]
2. Alexander, C.; Moeslund, J.E.; Bøcher, P.K.; Arge, L.; Svenning, J.-C. Airborne laser scanner (LiDAR) proxies for understory light conditions. *Remote Sens. Environ.* **2013**, *134*, 152–161. [CrossRef]
3. Mücke, W.; Hollaus, M. Modelling light conditions in forests using airborne laser scanning data. In Proceedings of the SilviLaser 2011, 11th International Conference on LiDAR Applications for Assessing Forest Ecosystems, University of Tasmania, Hobart, TAS, Australia, 16–20 October 2011; Volume 2011.
4. Durand, M.; Murchie, E.H.; Lindfors, A.V.; Urban, O.; Aphalo, P.J.; Robson, T.M. Diffuse solar radiation and canopy photosynthesis in a changing environment. *Agric. For. Meteorol.* **2021**, *311*, 108684. [CrossRef]
5. Welles, J.M.; Cohen, S. Canopy structure measurement by gap fraction analysis using commercial instrumentation. *J. Exp. Bot.* **1996**, *47*, 1335–1342. [CrossRef]
6. Lieffers, V.J.; Messier, C.; Standt, K.J.; Gendron, F.; Comeau, P.G. Predicting and managing light in the understory of boreal forests. *Can. J. For. Res.* **1999**, *29*, 796–811. [CrossRef]
7. Englund, S.R.; O'brien, J.J.; Clark, D.B. Evaluation of digital and film hemispherical photography and spherical densiometry for measuring forest light environments. *Can. J. For. Res.* **2000**, *30*, 1999–2005. [CrossRef]
8. Peng, S.; Zhao, C.; Xu, Z. Modeling spatiotemporal patterns of understory light intensity using airborne laser scanner (LiDAR). *ISPRS J. Photogramm. Remote Sens.* **2014**, *97*, 195–203. [CrossRef]
9. Angelini, A.; Corona, P.; Chianucci, F.; Portoghesi, L. Structural attributes of stand overstory and light under the canopy. *CRA J.* **2015**, *39*, 23–31.
10. Moeser, D.; Roubinek, J.; Schleppi, P.; Morsdorf, F.; Jonas, T. Canopy closure, LAI and radiation transfer from airborne LiDAR synthetic images. *Agric. Forest Meteorol.* **2014**, *197*, 158–168. [CrossRef]
11. Comeau, P. *Measuring Light in the Forest*; Technical Report; Ministry of Forests: Victoria, BC, Canada, 2000.
12. Promis, Á. Measuring and estimating the below-canopy light environment in a forest: A Review. In *Revista Chapingo Serie Ciencias Forestales y del Ambiente*; Universidad Autónoma Chapingo: Chapingo, Mexico, 2013; Volume XIX, pp. 139–146.
13. Olpenda, A.S.; Stereńczak, K.; Będkowski, K. Modeling solar radiation in the forest using remote sensing data: A review of approaches and opportunities. *Remote Sens.* **2018**, *10*, 694. [CrossRef]
14. Vosselman, G.; Maas, H.G. Airborne and terrestrial laser scanning. *Int. J. Digit. Earth* **2010**, *4*, 183–184.
15. Lemmens, M. Terrestrial laser scanning. In *Geotechnologies and the Environment*; Springer: Dordrecht, The Netherland, 2011; pp. 101–121.
16. Farhan, S.M.; Yin, J.; Chen, Z.; Memon, M.S. A comprehensive review of LiDAR applications in crop management for precision agriculture. *Sensors* **2024**, *24*, 5409. [CrossRef] [PubMed]
17. Wu, D.; Johansen, K.; Phinn, S.; Robson, A. Suitability of airborne and terrestrial laser scanning for mapping tree crop structural metrics for improved orchard management. *Remote Sens.* **2020**, *12*, 1647. [CrossRef]
18. Neuville, R.; Bates, J.S.; Jonard, F. Estimating forest strucsture from UAV-mounted LiDAR point cloud using machine learning. *Remote Sens.* **2021**, *13*, 352. [CrossRef]
19. Li, X.; Liu, C.; Wang, Z.; Xie, X.; Li, D.; Xu, L. Airborne LiDAR: State-of-the-art of system design, technology and application. *Meas. Sci. Technol.* **2020**, *32*, 032002. [CrossRef]
20. Moudrý, V.; Cord, A.F.; Gábor, L.; Laurin, G.V.; Barták, V.; Gdulová, K.; Malavasi, M.; Rocchini, D.; Stereńczak, K.; Prošek, J.; et al. Vegetation structure derived from airborne laser scanning to assess species distribution and habitat suitability: The way forward. *Divers Distrib.* **2014**, *29*, 39–50. [CrossRef]
21. Bode, C.A.; Limm, M.P.; Power, M.E.; Finlay, J.C. Subcanopy Solar Radiation model: Predicting solar radiation across a heavily vegetated landscape using LiDAR and GIS solar radiation models. *Remote Sens. Environ.* **2014**, *154*, 387–397. [CrossRef]
22. Morsdorf, F.; Kötz, B.; Meier, E.; Itten, K.; Allgöwer, B. Estimation of LAI fractional cover from small footprint airborne laser scanning data based on gap fraction. *Remote Sens. Environ.* **2006**, *104*, 50–61. [CrossRef]
23. Lefsky, M.A.; Cohen, W.B.; Parker, G.G.; Harding, D.J. Lidar Remote Sensing for Ecosystem Studies. *BioScience* **2002**, *52*, 19–30. [CrossRef]
24. Shan, J.; Toth, C.H.K. *Topographic Laser Ranging and Scanning*, 1st ed.; CRC Press: Boca Raton, FL, USA, 2009; p. 590.
25. Dandoisa, J.P.; Ellis, E.C. Remote sensing of vegetation structure using computer vision. *Remote Sens.* **2010**, *2*, 1157–1176. [CrossRef]

26. Witzmann, S.; Gollob, C.H.; Kraßnitzer, R.; Ritter, T.; Tockner, A.; Schume, H.; Northdurft, A. Modeling of solar radiation and sub-canopy light regime on forest inventory plots of mixed conifer and deciduous temperate forests using point clouds from personal laser scanning. *For. Ecol. Manag.* **2024**, *569*, 122166. [CrossRef]
27. Xue, X.; Jin, S.; An, F.; Eichhorn, M.O.; Jin, C.H.; Chen, B.; Jiang, L.; Yun, T. Shortwave radiation Calculation for forests plots using airborne LiDAR data and computer graphics. *Plant Phenomics* **2022**, *2022*, 9856739. [CrossRef] [PubMed]
28. Zhang, Y.; Feng, X.; Chang, X.; Tie, L. Impacts of canopy structure on the sub-canopy solar radiation under a deciduous forest based on fisheye photographs. *Res. Cold Arid. Reg.* **2023**, *15*, 150–160. [CrossRef]
29. Sahu, B.K.; Jena, P. Based on fisheye images, effects of canopy structure on sub-canopy solar radiation within an evergreen forest. *Juni Khyat* **2020**, *10*, 379–399.
30. Šúri, M.; Hofierka, J. A new GIS-based solar radiation model and its application to photovoltaic assessments. *Trans. GIS* **2004**, *8*, 175–190. [CrossRef]
31. Neteler, M.; Mitasova, H. *Open Source GIS: A GRASS GIS Approach*, 3rd ed.; Springer: New York, NY, USA, 2008.
32. Fu, P.; Rich, P.M. *The Solar Analyst 1.0 User Manual*; Helios Environmental Modeling Institute: Lawrence, KS, USA, 2000; p. 53.
33. Pružinec, F.; Ďuračiová, R. A Point-Cloud Solar Radiation Tool. *Energies* **2022**, *15*, 7018. [CrossRef]
34. Parker, G.G.; Harding, D.J.; Berger, M.L. A portable LIDAR system for rapid determination of forest canopy structure. *J. Appl. Ecol.* **2004**, *41*, 755–767. [CrossRef]
35. GRASS GIS. What Is GRASS GIS. Available online: https://grass.osgeo.org/learn/overview/ (accessed on 16 June 2024).
36. Rigollier, C.H.; Bauer, O.; Wald, L. On the clear sky model of the ESRA—European Solar Radiation Atlas—With respect to the heliosat method. *Sol. Energy* **2000**, *68*, 33–48. [CrossRef]
37. Solar Radiation Data. Linke Turbidity (Tl) Factor Worldwide. Available online: https://www.soda-pro.com/help/general-knowledge/linke-turbidity-factor (accessed on 19 December 2024).
38. ÚGKK 2024. Office of Geodesy, Cartography and Cadastre of the Slovak Republic—Airborne Laser Scanning Data. Available online: https://www.geoportal.sk/sk/zbgis/lls/ (accessed on 5 May 2024).